Ocean Engineering 352 (2026) 124474



Contents lists available at ScienceDirect

Ocean Engineering

journal homepage: www.elsevier.com/locate/oceaneng



Research paper

An efficient SPH-FEM model for three-dimensional fluid-structure interactions via direct particle-surface mesh coupling

Xiang-Shan Guan [a], Peng-Nan Sun [b,*], Xiong Zhang [a], Xin-Yun Ni [c], Chun-Mei Xie [c]

[a] School of Aerospace Engineering, Tsinghua University, Beijing, 100084, China
[b] School of Ocean Engineering and Technology, Sun Yat-sen University & Southern Marine Science and Engineering Guangdong Laboratory, Zhuhai, 519082, China
[c] China Ship Scientific Research Center, Wuxi, 214082, China

ARTICLE INFO

Keywords:
Smoothed particle hydrodynamics
Finite element method
Single-layer particle boundary algorithm
Fluid-structure interaction
SPH-FEM Coupling model

ABSTRACT

The precise simulation of three-dimensional fluid-structure interaction (FSI) phenomena has always been a hot topic in computational mechanics. To solve FSI problems, a bidirectional coupling strategy technique between the Smoothed Particle Hydrodynamics (SPH) method and Finite Element Method (FEM) is proposed based on a single-layer particle boundary technique in this paper, enabling efficient three-dimensional coupling between fluid particles and solid elements. Within the proposed SPH-FEM coupling framework, a mapping relationship is constructed between surface meshes and single-layer SPH particles, where the surface meshes share nodes with solid elements to transmit external loads. At the same time, the single-layer particles serve as solid boundaries for the SPH solver. The approach eliminates the need for additional boundary treatments and node arrangements required in conventional SPH-FEM coupling algorithms, significantly improving data exchange efficiency between the SPH and FEM modules. The model introduces a boundary shield algorithm and permits different particle/mesh resolutions at the fluid-structure interface, enabling the simulation of three-dimensional FSI problems with complex geometries. Afterwards, the improved SPH-FEM coupling model is adopted to carry out numerical simulations of typical FSI problems, such as the water impact of a wedge, the deformation of an elastic plate under dam-break flows, the flexible floating body under dam-break flows, and the dynamic response of a flexible ship under waves. The numerical results are compared and verified with reference results, proving the computational accuracy of the SPH-FEM coupling algorithm in the FSI problem and broadening the application prospects of the SPH method in engineering problems.

1. Introduction

In computational mechanics and engineering applications, fluid-structure interaction (FSI) phenomena characterized by large deformations, strong nonlinearities, and multi-material interactions are prevalent across marine engineering, aerospace systems, and geohazard simulations (Groenenboom and Siemann, 2015; Siemann and Langrand, 2017). Such problems typically involve complex physical processes, including violent fluid impacts, free-surface evolution, and coupled structural responses (Zhang et al., 2021b), posing significant challenges for numerical methods in balancing accuracy, stability, and computational efficiency (Groenenboom and Siemann, 2015; Zhang et al., 2017). Consequently, the numerical simulation of complex FSI problems remains a critical research challenge in computational mechanics and engineering problems.

To address complex FSI problems, researchers have developed various numerical approaches, among which mesh-based methods have long dominated the field, including Finite Volume Method (FVM) (Barth et al., 2018), Finite Element Method (FEM) (Bathe, 2007), and Finite Difference Method (FDM) (Huang et al., 2019). Having been developed over several decades, these mesh-based approaches possess rigorous mathematical foundations and well-established numerical analysis theories, with comprehensive studies on their stability, convergence, and error estimation characteristics. However, such methods face inherent challenges when handling moving boundaries and extreme free-surface deformations, which significantly limit their flexibility in FSI simulations. The Arbitrary Lagrangian-Eulerian (ALE) method has emerged as a primary approach for FSI numerical modeling (Kjellgren and Hyvärinen, 1998; Basting et al., 2017; Jacob et al., 2021), which employs separate fluid and structural meshes to simulate different phases. Nevertheless,

* Corresponding author.
E-mail addresses: guanxs@mail.tsinghua.edu.cn (X.-S. Guan), sunpn@mail.sysu.edu.cn (P.-N. Sun), xzhang@mail.tsinghua.edu.cn (X. Zhang), nixinyun@cssrc.com.cn (X.-Y. Ni), xiechunmei@cssrc.com.cn (C.-M. Xie).

https://doi.org/10.1016/j.oceaneng.2026.124474
Received 13 November 2025; Received in revised form 24 January 2026; Accepted 27 January 2026
Available online 4 February 2026
0029-8018/© 2026 Elsevier Ltd. All rights are reserved, including those for text and data mining, AI training, and similar technologies.

frequent remeshing of the fluid domain is often required in simulations involving complex structural configurations, substantially increasing the computational complexity of numerical simulations.

Meshless methods demonstrate distinct advantages (Hwang et al., 2016; Sun et al., 2021; Gotoh et al., 2021; Sun et al., 2017; Khayyer et al., 2022a; Zhang et al., 2024) in simulating FSI problems characterized by large deformations, moving boundaries, and multi-material systems. Compared to conventional Eulerian mesh-based approaches, meshless methods can more naturally handle complex boundary variations and multi-material interactions, making them particularly suitable for free-surface flows, FSI problems, and multi-phase interactions. Currently, the typical meshless methods include the Smoothed Particle Hydrodynamics (SPH) method and the Moving Particle Semi-implicit (MPS) method (Li et al., 2020). The SPH method was originally proposed by Gingold and Monaghan (1977) and Lucy (1977) for simulating non-axisymmetric phenomena in astrophysics. However, owing to its unique meshless nature and Lagrangian formulation, the SPH method was soon introduced into fluid mechanics and has undergone significant development, emerging as an important approach for fluid simulations (Liu and Zhang, 2019; Liu and Liu, 2010). The core concept of the SPH method lies in its kernel approximation theory, which discretizes the governing equations of fluid dynamics through particle approximation. In the SPH framework, each particle carries independent physical properties and evolves according to fluid dynamics principles within a Lagrangian framework. SPH method directly characterizes fluid dynamic behavior through particle motion, thereby exhibiting remarkable advantages in continuum mechanics problems involving large deformations, moving boundaries, strong convection, and multi-phase coupling (Domínguez et al., 2022; Guan et al., 2024a; Lyu et al., 2021; Liu et al., 2025; Wu et al., 2025).

Over nearly five decades of development, the SPH method has achieved significant advancements in both theoretical frameworks and numerical algorithms, with marked improvements in computational accuracy and stability. Particularly in areas such as numerical dissipation control, boundary treatment, and particle repositioning for complex flow fields, researchers have proposed various enhancement schemes, rendering SPH more efficient and precise for simulating complex flow phenomena (Antuono et al., 2010; Crespo et al., 2015; Cercos-Pita, 2015; Lyu et al., 2022; Xu et al., 2025).

The maturation of the Total Lagrangian SPH (TLSPH) model has notably advanced the capability in simulating elastic responses. Numerous researchers have made outstanding contributions to TLSPH algorithms for FSI problems (Khayyer et al., 2018b,a; Shimizu et al., 2022). Khayyer et al. (2022b) developed a fully meshless 3D solver for hydroelastic problems by coupling SPH with Hamiltonian formulations, extending its capability through anisotropic composite structure simulations. Sun et al. (2021) integrated the δ^+-SPH model with the TLSPH framework to establish an FSI-SPH model for elastic bodies, employing multi-resolution discretization in the fluid domain and maintaining uniform spatial resolution at fluid-structure interfaces. Additionally, SPH-based FSI solvers with different resolution configurations for fluids and solids have been developed and validated against benchmark cases (Khayyer et al., 2021).

However, the conventional approach of using single-resolution particles for solid elasticity simulation leads to excessive particle counts in solids (Zhang et al., 2011). Furthermore, the time step limited by sound speed in solid simulations remains restrictive, posing challenges for full-scale 3D elastic structure simulations. Compared to traditional mesh-based methods, SPH still exhibits gaps in both accuracy and computational efficiency (Vacondio et al., 2021; Chen et al., 2022).

The FEM, with its well-established theoretical foundation and high precision, has been widely adopted in solid mechanics and structural dynamics (Bathe, 2007). However, FEM encounters substantial difficulties when handling large fluid deformations, topological changes, and free surfaces - particularly requiring frequent remeshing under severe element distortion. Consequently, coupled SPH-FEM approaches have emerged as a promising solution for simulating FSI problems (De Vuyst et al., 2005).

Both SPH and FEM belong to the Lagrangian framework, inherently capable of tracking material motion and deformation. The shared characteristic provides a unified kinematic description and facilitates efficient data transfer mechanisms for their coupling, making SPH-FEM hybrid approaches particularly valuable for multi-physics and multi-scale simulations (Hermange et al., 2019; Yao et al., 2023). As a meshless method, SPH demonstrates superior capability in handling large fluid deformations, free-surface flows, and complex boundary conditions (Antuono et al., 2010; Zhang et al., 2021a). Conversely, FEM excels in modeling small deformations, structural mechanics, and precise boundary enforcement (Huebner et al., 2001). Their synergistic integration enables the SPH-FEM algorithm to simultaneously resolve large-scale fluid motions and fine-scale structural deformations, thereby achieving multi-scale and multi-physics FSI simulations (Marrone et al., 2016). The coupled SPH-FEM algorithm not only effectively addresses complex fluid-structure interactions but also achieves an optimal balance between computational efficiency and numerical accuracy (Zhang et al., 2011).

SPH-FEM coupling algorithms have achieved significant advancements in recent years (Yao et al., 2023; Li et al., 2024). The most commonly used SPH-FEM coupling strategy at present is the contact force method, also known as the master-slave contact algorithm. Johnson (1994) implemented a rigid coupling scheme that fixes SPH particles to adjacent FEM nodes, with stresses at the interface computed using neighboring particles and interfacial particles. The algorithm typically employs a penalty function method to apply contact forces at the fluid-structure interface, preventing SPH particles from penetrating finite elements. It has been widely implemented in commercial software such as LS-DYNA for solving a range of full-scale complex engineering problems (Groenenboom et al., 2019; Topalović et al., 2021), including bridge blasting simulations (Karmakar and Shaw, 2021; Saha and Karmakar, 2025), debris flow impacting bridges (Yao et al., 2024), and marine structure collisions (Hasanpour et al., 2021).

De Vuyst et al. (2005) proposed an alternative method that treats FEM nodes as SPH particles, introducing a particle contact algorithm to directly compute interaction forces between nodes and particles. Compared to master-slave contact algorithm, this approach simplifies implementation by eliminating the need for explicit contact surface construction or normal vector calculations. After that, Fourey et al. (2017) proposed a high-accuracy SPH-FEM coupling model by generating fixed-ghost particles at the coupling interface. Based on the work of Fourey et al. (2017), Hermange et al. (2019) extended this SPH-FEM coupling model to three-dimensional engineering problems, achieving simulations of tire water-splashing. Fuchs et al. (2021) introduced a novel SPH-FEM coupling strategy based on a Dirichlet-Neumann partitioned approach to facilitate information exchange between the fluid and solid domains. Zhang et al. (2021c) developed a new virtual particle coupling strategy for SPH and FEM, which proves highly effective for simulating violent sloshing involving deformable baffles or container walls with variable geometry.

The approaches mentioned above often require additional particle arrangements at the SPH-FEM fluid-structure interface to ensure robustness in SPH computations, which generally leads to modeling the interface with multiple layers of elements or particles. However, modeling complex structures such as thin-walled components poses significant challenges in engineering applications, as excessively fine mesh or particle sizes tend to result in prohibitively high computational costs(Shi et al., 2026). Therefore, (Caleyron et al., 2013) proposed a novel SPH-FEM coupling model, which for the first time adopted a single-layer particle boundary to discretize thin-walled structures. Chen et al. (2022) developed a flux-based coupling method using a single-layer particle boundary algorithm, incorporating multi-resolution discretization for fluid and structure domains. The accuracy of the algorithm was systematically validated through 2D benchmarks. Subsequently,

Gao and Fu (2024) extended the single-layer particle boundary approach to fluid-shell interaction by proposing a three-dimensional meshless framework based on SPH coupled with semi-meshless thin shells. Shi et al. (2026) presented a 3D SPH-FEM coupling model for modeling FSI problems based on the single-layer particle boundary technique, where Mindlin-Reissner shell elements are employed in FEM for structural modeling to reduce geometric complexity and improve computational efficiency. Chen et al. (2025) conducted similar work, employing a degenerated continuum theory to describe the dynamic behavior of the shell structure, and applied it to the simulation of a three-dimensional ship hull section water entry.

Currently, full-scale SPH-FEM coupling simulations for three-dimensional solid elements primarily rely on commercial software based on the contact force method (Groenenboom et al., 2019; Guan et al., 2023) or employ additional virtual particle techniques (Hermange et al., 2019). Research on three-dimensional SPH-FEM coupling using a single-layer particle boundary has largely focused on fluid-shell interactions (Gao and Fu, 2024; Shi et al., 2026), while its application to coupling with three-dimensional solid elements remains relatively limited. Therefore, an enhanced SPH-FEM coupling model based on an improved single-layer particle boundary algorithm (Guan et al., 2024b) is proposed in this paper, which is well-suited for solving three-dimensional FSI problems in hydrodynamic scenarios. The surface mesh of solid elements directly serves as the single-layer particle boundary for the SPH domain, while the forces exerted by SPH fluid particles on boundaries are interpolated as surface loads for FEM computation. Notably, the information transfer and interpolation at fluid-structure interfaces are achieved without requiring additional virtual particles, significantly simplifying the complexity of the algorithm and improving the efficiency of SPH-FEM data exchange at complex elastic boundaries. Furthermore, the model introduces a boundary shield algorithm and allows for different particle and mesh resolutions at the fluid-structure interface (Guan et al., 2024b), which enhances its capability to solve full-scale three-dimensional FSI problems with complex geometries in hydrodynamic scenarios. The proposed method has been rigorously validated through a series of three-dimensional benchmarks, demonstrating its superior computational accuracy and efficiency in solving FSI problems.

This paper is structured as follows: Section 2 introduces the SPH model, FEM algorithm, and coupling strategy employed in this work. Section 3 validates the improved SPH-FEM coupling algorithm through three benchmark cases: water impact of a wedge, impact of dam-break flow on an elastic baffle, and motion of a flexible floating structure under dam-break flow. The numerical results demonstrate excellent agreement with reference data, confirming the computational accuracy of the proposed coupling model. Furthermore, the enhanced SPH-FEM approach is successfully applied to simulate a scaled ship model subjected to wave impact in Section 4, demonstrating its capability for solving large-scale complex FSI problems. Finally, Section 5 summarizes the key conclusions and discusses potential research directions.

2. SPH-FEM Coupling model

2.1. SPH Model of fluid domain

Fluids are typically treated as nearly incompressible in most applications, as density variations are generally minimal. Building on this concept, Monaghan and Gingold (1983) developed the Weakly-Compressible Smoothed Particle Hydrodynamics (WCSPH) method by using a density-based state equation to compute pressure. However, early WCSPH implementations revealed significant pressure oscillations in liquid simulations due to the weak compressibility assumption. To address this issue, researchers have proposed various enhanced WCSPH formulations that reduce pressure fluctuations. As highlighted by Sun et al. (2023), one particularly effective approach is the δ-SPH model introduced by Antuono et al. (2010), whose governing equations are presented below:

$$\begin{cases} \frac{D\rho_i}{Dt} = -\rho_i \sum_j \left(\boldsymbol{u}_j - \boldsymbol{u}_i\right) \cdot \nabla_i W_{ij} V_j + \delta h c_0 D_i \,, \\ \frac{D\boldsymbol{u}_i}{Dt} = -\frac{1}{\rho_i} \sum_j \left(p_i + p_j\right) \nabla_i W_{ij} V_j + \frac{\boldsymbol{F}_i^{ad}}{\rho_i} + \boldsymbol{g} + \alpha_1 h c_0 \frac{\rho_0}{\rho_i} \sum_j \pi_{ij} \nabla_i W_{ij} V_j \,, \\ \frac{D\boldsymbol{r}_i}{Dt} = \boldsymbol{u}_i \,, p = c_0^2 \left(\rho - \rho_0\right) \,, \\ D_i = 2 \sum_j \psi_{ji} \left(\boldsymbol{r}_j - \boldsymbol{r}_i\right) \cdot \nabla_i W_{ij} V_j / \left|\boldsymbol{r}_j - \boldsymbol{r}_i\right|^2 \,, \\ \pi_{ij} = \left(\boldsymbol{u}_j - \boldsymbol{u}_i\right) \cdot \left(\boldsymbol{r}_j - \boldsymbol{r}_i\right) / \left|\boldsymbol{r}_j - \boldsymbol{r}_i\right|^2 \,, \\ \boldsymbol{F}_i^{ad} = \alpha_2 \rho_0 c_0 h \langle \nabla(\nabla \cdot \boldsymbol{u}(\boldsymbol{r})) \rangle_i = \alpha_2 \rho_0 c_0 h \sum_j (K_j + K_i) \nabla_i W_{ij} V_j \,, \\ K_i = \langle \nabla \cdot \boldsymbol{u} \rangle_i = \sum_j \boldsymbol{u}_{ji} \cdot \nabla_i W_{ij} V_j \,, \\ \psi_{ij} = \left(\rho_j - \rho_i\right) - 0.5 \left[\langle \nabla \rho \rangle_i^L + \langle \nabla \rho \rangle_j^L \right] \cdot \left(\boldsymbol{r}_j - \boldsymbol{r}_i\right) \,. \end{cases} \tag{1}$$

In the governing equations, ρ and ρ_0 denote the current and reference densities of fluid particles, V represents particle volume, p indicates hydrodynamic pressure, and D/Dt stands for the material (Lagrangian) time derivative. $\boldsymbol{u}$ and $\boldsymbol{r}$ correspond to particle velocity and position, where subscripts i and j identify central and neighboring particles respectively. W is the kernel function with h as its smoothing length, and $\boldsymbol{g}$ represents gravitational acceleration (Lyu et al., 2024).

The term located at the far right of the continuity equation describes density diffusion, while the right term of the momentum equation is artificial viscosity. According to Antuono et al. (2012), the parameter δ generally adopts a fixed value of 0.1 across different scenarios. The concept of artificial viscosity was first proposed by Monaghan and Gingold (1983), and it contributes to a more uniform distribution of particles in the flow field, enhancing the precision of particle approximation.

The value of α_1 follows the suggestions in literature (Guan et al., 2024a; Sun et al., 2021), which is set to 0.1. Additionally, Sun et al. (2023) proposed the acoustic damper term ($\boldsymbol{F}_i^{ad}$), which can suppress pressure oscillations and leads to a smoother pressure field. Studies in Sun et al. (2023) confirm that the coefficient α_2 can range from 0 to 1 without altering the time step size, and α_2 is set to 0.5 in this paper.

c_0 serves as a crucial adjustable parameter in the weakly compressible assumption. The selection of c_0 requires careful consideration: an undersized value compromises the weakly compressible assumption, while an excessive value significantly increases computational cost due to the direct correlation between c_0 and the time step size in WCSPH methods. For computational efficiency, artificial sound speed is generally adopted instead of physical sound speed. Monaghan (2005) demonstrated that setting c_0 at 10 times the maximum flow velocity effectively maintains density variations below 1%, thereby preserving the weakly compressible condition. Furthermore, under scenarios involving violent impacts or substantial hydrostatic pressure, an additional constraint $c_0 \geq 10\sqrt{p_{\max}/\rho_0}$ is adopted (Antuono et al., 2011). Therefore, the artificial sound speed is determined by the following equation:

$$c_0 \geq 10 \max(U_{\max}, \sqrt{p_{\max}/\rho_0}) \,, \tag{2}$$

where $U_{\max}$ and $p_{\max}$ represent the estimated maximum flow velocity and pressure, respectively. $U_{\max}$ is calculated based on the peak velocity of moving bodies in the simulation, while $p_{\max}$ is derived from the hydrostatic pressure at the deepest fluid region.

In practical computations, the kernel function W is conventionally considered to vanish when $|\boldsymbol{x} - \boldsymbol{y}| > kh$, where kh defines the support domain radius of W. Following the Wendland kernel function (Wendland, 1995) adopted in this study, the coefficient k is set to 2, and h is uniformly specified as 1.25 times the initial fluid particle spacing throughout our simulations.

When the support domain of W is bounded, it can be decomposed into two distinct regions: the computational domain $\mathbb{R}$ and the boundary domain $\partial\mathbb{R}$. As illustrated in Fig. 1, the outer normal vector of boundaries is specified as pointing toward the fluid domain. Under such truncation conditions, the SPH interpolation formula can be written as

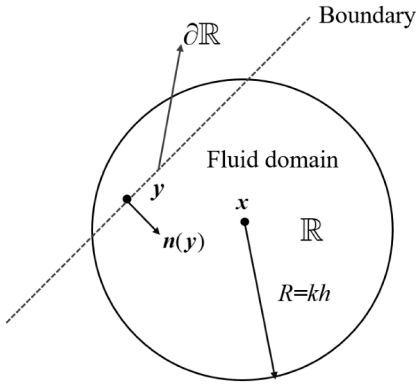


Fig. 1. Sketch of SPH kernel approximate support domain.

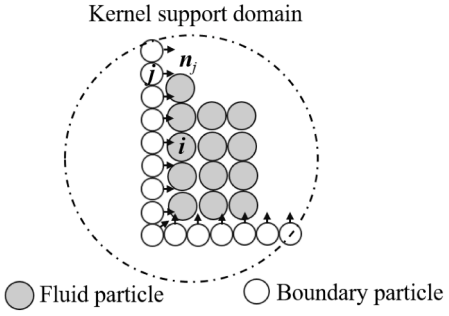


Fig. 2. Sketch of single-layer particle boundary.

(Cercos-Pita, 2015):

$$\langle f(\boldsymbol{x})\rangle = \frac{1}{\gamma(\boldsymbol{x})}\int_{\boldsymbol{y}\in\mathbb{R}} f(\boldsymbol{y})W(\boldsymbol{x}-\boldsymbol{y})d\boldsymbol{y}\,, \tag{3}$$

$$\begin{aligned}\langle \nabla f(\boldsymbol{x})\rangle =& \frac{1}{\gamma(\boldsymbol{x})}\int_{\boldsymbol{y}\in\mathbb{R}} f(\boldsymbol{y})\nabla W(\boldsymbol{y}-\boldsymbol{x})d\boldsymbol{y}\\ &-\frac{1}{\gamma(\boldsymbol{x})}\int_{\boldsymbol{y}\in\partial\mathbb{R}} f(\boldsymbol{y})\boldsymbol{n}(\boldsymbol{y})W(\boldsymbol{y}-\boldsymbol{x})d\boldsymbol{y}\,,\end{aligned} \tag{4}$$

where $\gamma(\boldsymbol{x})$ is the Shepard normalization factor and defined as:

$$\gamma(\boldsymbol{x}) = \int_{\boldsymbol{y}\in\mathbb{R}} W(\boldsymbol{x}-\boldsymbol{y})d\boldsymbol{y}\,. \tag{5}$$

The single-layer particle boundary algorithm can discretize structures into a single layer of boundary particles. Compared to conventional fixed-ghost particle methods, this approach requires fewer particles but necessitates additional geometric information. Specifically, accurate computation of the kernel truncation effects at fluid-boundary interfaces requires both normal vectors and surface area information for each boundary particle (Chen et al., 2021). A schematic representation of this technique is provided in Fig. 2.

The SPH method constructs its integration domain through discrete particles, where the computational domain is represented by fluid particles and boundaries are discretized using single-layer particles. Through particle approximation, the integral form of the kernel function can be converted into a discrete summation formulation, which is shown in Eq. (6).

$$\begin{cases}\gamma_i = \sum_{j\in F} W_{ij}V_j\\ \langle f\rangle_i = \frac{1}{\gamma_i}\sum_{j\in B} f_j W_{ij}V_j\,,\\ \langle \nabla f\rangle_i = \frac{1}{\gamma_i}\left(\sum_{j\in F} f_j\nabla_i W_{ij}V_j - \sum_{j\in B} f_j\boldsymbol{n}_j W_{ij}S_j\right),\end{cases} \tag{6}$$

The equations are defined within the fluid domain F and boundary B, where $\boldsymbol{n}_j$ and S indicates the outward normal vector and area of boundary particles.

Therefore, by reformulating the governing equations of the δ-SPH model according to Eq. (6), the following modified continuity and momentum equations that properly account for support domain truncation effects can be obtained (Guan et al., 2024b):

$$\begin{aligned}\frac{D\rho_i}{Dt} =& -\frac{1}{\gamma_i}\rho_i\sum_{j\in F}(\boldsymbol{u}_j-\boldsymbol{u}_i)\cdot\nabla_i W_{ij}V_j + \delta hc_0 D_i\\ &+\frac{1}{\gamma_i}\sum_{j\in B}\rho_j(\boldsymbol{u}_j-\boldsymbol{u}_i)\cdot\boldsymbol{n}_j W_{ij}S_j\,,\end{aligned} \tag{7}$$

$$\begin{aligned}\frac{D\boldsymbol{u}_i}{Dt} =& -\frac{1}{\gamma_i}\sum_{j\in F}\left(\frac{p_i+p_j}{\rho_i}\right)\nabla_i W_{ij}V_j + \boldsymbol{g} + \frac{1}{\rho_i}\boldsymbol{F}_i^{ad}\\ &+\frac{1}{\rho_i}\alpha hc_0\rho_0\sum_{j\in F}\pi_{ij}\nabla_i W_{ij}V_j\\ &+\frac{1}{\gamma_i}\sum_{j\in B}\left(\frac{p_i+p_j}{\rho_i}\right)\boldsymbol{n}_j W_{ij}S_j\,.\end{aligned} \tag{8}$$

The physical interpretations of the parameters in Eq. (7) and Eq. (8) remain consistent with those in Eq. (1). When boundary terms vanish and γ_i equals 1, these equations reduce to the form of Eq. (1).

The pressure of boundary particles can be obtained by interpolation of fluid particles (Guan et al., 2024b), which can be calculated as:

$$p_j = \frac{\sum_{j\in F}\left[p_i+\rho_i(\boldsymbol{a}_j-\boldsymbol{g})\cdot\boldsymbol{r}_{ij}\right]W_{ij}}{\sum_{i\in F}W_{ij}}, j\in B\,, \tag{9}$$

where $\boldsymbol{a}_j$ is the acceleration of solid particles.

The time step for the SPH module can be determined according to the following formula:

$$\begin{cases}\Delta t_a = 0.25\min_i\sqrt{\left|\frac{h_i}{\boldsymbol{a}_i}\right|}, \quad \Delta t_c = \mathrm{CFL}\min_i\frac{h_i}{c_0}\,,\\ \Delta t = \min(\Delta t_a, \Delta t_c)\,,\end{cases} \tag{10}$$

where CFL denotes the Courant number, which is 1.25 in the simulations. The time integration scheme used for SPH simulations is explicit, which is the fourth-order Runge-Kutta (RK4) algorithm (Lyu et al., 2021).

When the geometry of structure boundaries is relatively simple, a uniform single-layer particle distribution can prevent the penetration of fluid particles. However, structural geometries are often highly complex in practical engineering problems, requiring finer particles to accurately represent these intricate surfaces. The adoption of a single-resolution particle arrangement for such complex boundaries may lead to an excessive number of particles. Consequently, adopting a multi-resolution single-layer particle distribution for complex boundary construction can significantly enhance computational efficiency.

Guan et al. (2024b) proposed an enhanced boundary shield technique, which improves the single-layer particle boundary method to maintain strong robustness even under multi-resolution particle distributions. The essence of the boundary shield algorithm lies in the application of a velocity correction to fluid particles that are about to penetrate the boundary. The expression for this velocity correction is given as follows:

$$\begin{cases}\delta\boldsymbol{u}_i = -\sum_{j\in B_k}(\boldsymbol{u}_i-\boldsymbol{u}_j)\cdot\mathbb{N}_j/N_k\,,\\ j\in B_k,\ \text{if}\ \left|\boldsymbol{r}_{ij}\right| < k_a d_0 \text{ and } \boldsymbol{r}_{ij}\cdot\boldsymbol{n}_j < k_b d_0 \text{ and } l<0\,,\\ \mathbb{N}_j = \boldsymbol{n}_j\otimes\boldsymbol{n}_j, l = (\boldsymbol{u}_i-\boldsymbol{u}_j)\cdot\boldsymbol{n}_j, \boldsymbol{r}_{ij} = \boldsymbol{r}_i-\boldsymbol{r}_j\,,\end{cases} \tag{11}$$

where d_0 denotes the maximum boundary particle spacing, and $\left|\boldsymbol{r}_{ij}\right|$ represents the particle distance. B_k indicates the boundary particles satisfying the specified conditions, while N_k denotes the number of boundary particles satisfying the specified conditions. k_a and k_b represent two criterion parameters, respectively. The criterion $l<0$ can ensure that only

fluid particles that are about to cross the boundary will be subjected to the velocity correction.

The boundary shield technique is not only applicable to multi-resolution particle distributions, but also ensures computational robustness when dealing with thin-walled structures. The particle size for constructing thin-walled boundaries is smaller, and the normal of particles on both sides of the thin-walled boundaries is opposite, so the kernel function scope of fluid particles can easily cross thin-walled boundaries. If there are fluid particles on the other side of the thin-walled boundary, the interpolation integral term of the fluid particles and boundary particles on the other side of the thin-walled boundary precisely will cancel out. If there are no fluid particles on the other side of the thin-walled boundary, the fluid particles may penetrate the boundary, but the boundary shield technique ensures the robustness of calculations.

Typically, k_a is set to a value less than 1 to ensure that velocity corrections are applied only to fluid particles in proximity to the solid boundary. Meanwhile, k_b determines the normal effective range of the velocity correction. Guan et al. (2024b) has demonstrated that the boundary shield algorithm has little impact on the momentum and energy conservation at interfaces. if k_a is taken as 0.75 and k_b as 0, the influence is negligible.

2.2. FEM Model of solid domain

In continuum mechanics, the space occupied by a deformable body at the initial time $t = 0$ is referred to as the initial configuration, while its occupied space at the current time is termed the current configuration. In our study, the updated Lagrangian formulation is selected for FEM calculations, where the reference configuration aligns with the current configuration (Bathe, 2007).

To facilitate the expression of governing equations, tensor index notation is introduced in this section. For instance, the position of a material point in the reference configuration can be expressed as:

$$\boldsymbol{X} = X_\alpha \boldsymbol{e}_\alpha\,,\quad \alpha = 1,2,3\,, \tag{12}$$

where $\boldsymbol{e}_\alpha$ denotes the basis vectors in the Cartesian coordinate system, and X_α represents the components of the position.

The governing equations of the updated Lagrangian framework are expressed as follows (Qian and Zhang, 1995):

$$\begin{cases} \rho(\boldsymbol{X},t)J(\boldsymbol{X},t) = \rho_0(\boldsymbol{X})\,, \\ \frac{\partial \sigma_{\beta\alpha}}{\partial x_\beta} + \rho f_\alpha = \rho a_\alpha\,, \\ \rho \dot{e} = D_{\alpha\beta}\sigma_{\alpha\beta}\,, \\ \sigma^\nabla = \sigma^\nabla(D_{\alpha\beta}, \sigma_{\alpha\beta}, \text{etc.})\,, \\ D_{\alpha\beta} = \frac{1}{2}\left(\frac{\partial v_\alpha}{\partial x_\beta} + \frac{\partial v_\beta}{\partial x_\alpha}\right), \end{cases} \tag{13}$$

where a_α denotes the acceleration components of material points in the current configuration, ρ represents the density, f_α indicates the body force components, v_α stands for velocity components, e is the specific internal energy, $\sigma_{\alpha\beta}$ represents the components of the Cauchy stress tensor, and $D_{\alpha\beta}$ denotes the components of the deformation rate tensor. σ^∇ signifies the objective stress rate used in constitutive relations. The Jaumann stress rate is suitable for solving explicit large rotation/strain problems. Due to the large rotation of solid deformation in benchmarks, the objective stress rate calculation in this algorithm adopts the Jaumann stress rate. J is the determinant of the deformation gradient tensor, which is named the Jacobian determinant and expressed as (Bathe, 2007):

$$J = \left|\frac{\partial x_\alpha}{\partial X_\beta}\right| = \begin{vmatrix} \frac{\partial x_1}{\partial X_1} & \frac{\partial x_1}{\partial X_2} & \frac{\partial x_1}{\partial X_3} \\ \frac{\partial x_2}{\partial X_1} & \frac{\partial x_2}{\partial X_2} & \frac{\partial x_2}{\partial X_3} \\ \frac{\partial x_3}{\partial X_1} & \frac{\partial x_3}{\partial X_2} & \frac{\partial x_3}{\partial X_3} \end{vmatrix}. \tag{14}$$

In the updated Lagrangian framework, the boundary conditions are specified as follows:

$$\begin{cases} \left(n_\beta \sigma_{\beta\alpha}\right)\Big|_{A_s} = \overline{f_\alpha}\,, \\ v_\alpha\Big|_{A_v} = \overline{v_\alpha}\,, \end{cases} \tag{15}$$

where $\overline{f_\alpha}$ represents the surface force acting on the deformed elements, A_s denotes the boundary of surface forces, and A_v indicates the velocity boundary. The boundary conditions provide essential kinematic and dynamic constraints for the motion and deformation of the continuum body.

After discretizing the deformable structure using finite elements, the displacement u_α at any point within an element can be interpolated from the nodal displacements $u_{\alpha i}(t)$ of element nodes, which is expressed as follows:

$$u_\alpha(x,y,z,t) = N_i(x,y,z)u_{\alpha i}(t)\,, \tag{16}$$

where i denotes the node index, which ranges from 1 to 8 for the eight-node hexahedral element. The $N_i(x,y,z)$ is the shape function of elements, and its matrix form of Eq. (16) is given by:

$$\boldsymbol{u} = \boldsymbol{N}\boldsymbol{u}^{fe}\,, \tag{17}$$

where fe represents the finite element, $\boldsymbol{N}$ is the shape function matrix, and $\boldsymbol{u}^{fe}$ denotes the nodal displacement matrix of finite elements.

The system equations of motion after finite element discretization can be expressed as follows:

$$\begin{cases} \boldsymbol{M}\boldsymbol{a}(t) + \boldsymbol{f}^{int} = \boldsymbol{f}^{ext}\,, \\ \boldsymbol{M}\boldsymbol{a}(t) + \boldsymbol{K}\boldsymbol{u}(t) = \boldsymbol{Q}(t)\,, \end{cases} \tag{18}$$

where $\boldsymbol{a}(t)$ and $\boldsymbol{u}(t)$ represent the nodal acceleration and displacement of the deformable body, respectively. $\boldsymbol{f}^{int}$ and $\boldsymbol{f}^{ext}$ denote the internal nodal force and external nodal force, while $\boldsymbol{M}$, $\boldsymbol{K}$, and $\boldsymbol{Q}$ correspond to the mass matrix, stiffness matrix, and load matrix of the deformable body, respectively. The system matrices are assembled from the element matrices of each finite element, with their specific expressions given below (Wu and Gu, 2012):

$$\boldsymbol{M} = \sum_{fe} \boldsymbol{M}^{fe}, \quad \boldsymbol{K} = \sum_{fe} \boldsymbol{K}^{fe}, \quad \boldsymbol{Q} = \sum_{fe} \boldsymbol{Q}^{fe}, \tag{19}$$

$$\begin{cases} \boldsymbol{M}^{fe} = \int_V \rho \boldsymbol{N}^T \boldsymbol{N}\, dV\,, \\ \boldsymbol{K}^{fe} = \int_V \boldsymbol{B}^T \boldsymbol{\sigma} \boldsymbol{B}\, dV\,, \\ \boldsymbol{Q}^{fe} = \int_V \boldsymbol{N}^T \boldsymbol{f}_v\, dV + \int_{S_\sigma} \boldsymbol{N}^T \boldsymbol{f}_s\, dS\,, \end{cases} \tag{20}$$

In the finite element formulation, $\boldsymbol{f}_v$ and $\boldsymbol{f}_s$ represent the body force and surface force, respectively. Given the known element shape function matrix $\boldsymbol{N}$, along with specified external loads, material density, and gravitational acceleration, both the element mass matrix $\boldsymbol{M}^{fe}$ and element load matrix $\boldsymbol{Q}^{fe}$ can be readily determined through direct computation. The primary computational challenge lies in the solution of the element stiffness matrix $\boldsymbol{K}^{fe}$, which fundamentally corresponds to the determination of the internal nodal forces $\boldsymbol{f}^{int}$.

In the expression of the element stiffness matrix $\boldsymbol{K}^{fe}$, $\boldsymbol{\sigma}$ represents the stress tensor, which is defined as:

$$\boldsymbol{\sigma} = [\sigma_{11} \quad \sigma_{22} \quad \sigma_{33} \quad \sigma_{23} \quad \sigma_{13} \quad \sigma_{12}]^T\,, \tag{21}$$

The element strain-displacement matrix $\boldsymbol{B}$ is constructed by assembling nodal strain-displacement matrices $\boldsymbol{B}_i$, analogous to the assembly of shape function matrices. The nodal strain-displacement matrix $\boldsymbol{B}_i$ for node i is expressed as:

$$\boldsymbol{B}_i = \begin{bmatrix} \frac{\partial N_i}{\partial X_1} & 0 & 0 & 0 & \frac{\partial N_i}{\partial X_3} & \frac{\partial N_i}{\partial X_2} \\ 0 & \frac{\partial N_i}{\partial X_2} & 0 & \frac{\partial N_i}{\partial X_3} & 0 & \frac{\partial N_i}{\partial X_1} \\ 0 & 0 & \frac{\partial N_i}{\partial X_3} & \frac{\partial N_i}{\partial X_2} & \frac{\partial N_i}{\partial X_1} & 0 \end{bmatrix}^T. \tag{22}$$

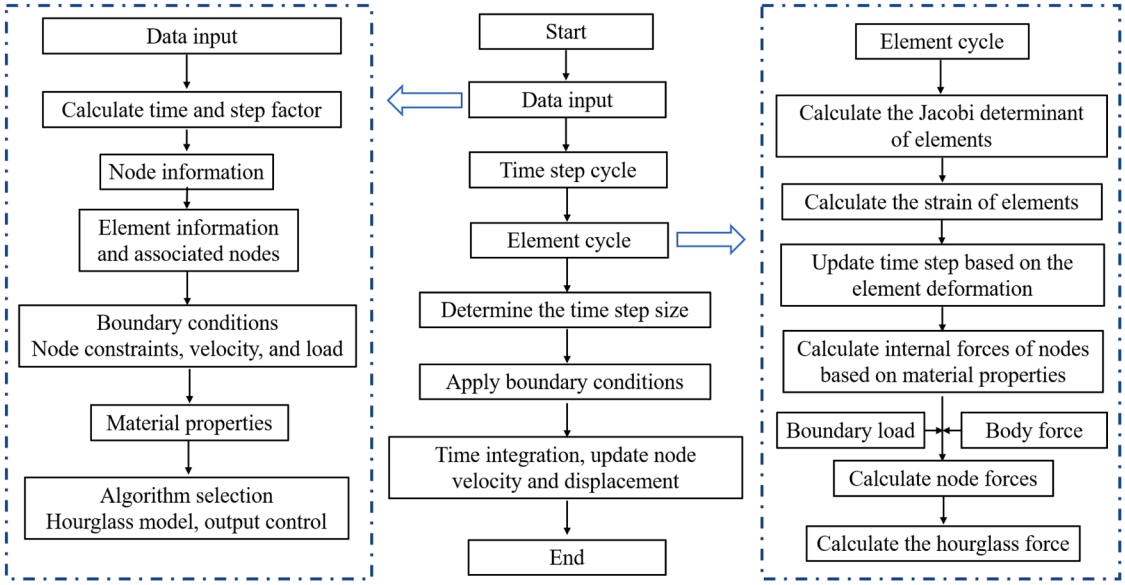


Fig. 3. Calculation process of finite element method.

After obtaining the node stiffness matrix, the element stiffness matrix can be obtained based on the stress tensor $\boldsymbol{\sigma}$, and then the internal forces can be solved. To ensure the computational stability of reduced integral units, the Flanagan Belytschko hourglass control algorithm (Flanagan and Belytschko, 1981) is adopted to apply hourglass force in the finite element module. If the ratio of hourglass energy to internal energy does not exceed 5%, then the calculation is stable.

In the present algorithm, the finite element module employs an explicit central difference method for time integration. The time step size in the central difference scheme is determined by the characteristic length of the finite elements. For large deformation problems of solids, where the characteristic length of finite elements undergoes significant changes, a variable time step central difference method must be adopted. The FEM time step size Δt_s is calculated as follows:

$$\begin{cases} \Delta t_s = \alpha_t \Delta t_{cr}, \\ \Delta t_{cr} = \min_e \frac{l_e}{c_e}, \end{cases} \tag{23}$$

where α_t is a constant step factor (typically taken as 0.9, with any value less than 1 being acceptable). c_e represents the sound speed in the finite element. For elastic materials, the wave speed c_e is calculated as $c_e = \sqrt{E(1-\nu)/[(1+\nu)(1-2\nu)\rho]}$, where E represents the Young modulus and ν denotes its Poisson ratio, while the characteristic element length l_e for an eight-node hexahedral element is defined as the ratio of the element volume to its maximum surface area, ensuring proper consideration of both material properties and geometric characteristics in the time integration scheme.

The complete calculation process of the finite element module is shown in Fig. 3.

2.3. SPH-FEM Coupling algorithm

In the FEM module, hexahedral solid elements are primarily employed to discretize elastic bodies with various geometric configurations. The quadrilateral facets of hexahedral elements serve as fluid-structure interfaces. The modeling of finite elements is mainly completed in Hypermesh. After generating solid elements, the face of solid components is extracted to generate surface meshes, so the solid elements and surface meshes share nodes, meaning all surface nodes are inherently contained within the solid element node set.

The SPH module utilizes the single-layer particle boundary algorithm to simulate solid walls, capable of constructing boundaries with arbitrary geometric complexity. During SPH-FEM coupling initialization, the single-layer particle boundary is directly interpolated from the FEM surface mesh, where the center of the surface mesh serves as the single-layer particle boundary for the SPH computational domain. The coupling interface between SPH domain and FEM elements is illustrated in Fig. 4.

In the SPH-FEM coupling process, the data transfer between SPH particles and FEM nodes is illustrated in Fig. 5. The FEM surface mesh, serving as the critical interface coupling the FEM elements with the SPH computational domain, not only shares nodes with the solid elements but also functions as the wall boundary for the SPH domain.

Within the SPH-FEM coupling framework, a mapping relationship is established between the FEM surface mesh and a single layer of SPH particles. The surface mesh array stores corresponding node indices, where the positions and velocities of nodes determine the positions and velocities of the associated SPH particles. Additionally, the connectivity sequence of the nodes dictates the normal vectors of the corresponding SPH particles, while the area of the quadrilateral surface elements defines the associated particle areas. At each time step of the SPH-FEM computation, the position, velocity, normal vector, and area of the SPH particles are dynamically generated based on the nodal information of the surface mesh. These data provide the boundary terms required for the interpolation calculations of SPH fluid particles.

Traditional SPH-FEM coupling methods often introduce additional particles or nodes at the interface, along with associated overhead for neighbor search and force mapping. In contrast, the present method directly maps the FEM surface mesh to SPH boundary particles, reducing interface data redundancy and simplifying force transfer.

The fluid force acting on a single-layer particle $\boldsymbol{F}_j$ can be obtained through the following formula:

$$\boldsymbol{F}_j = \sum_{i \in F} V_i (p_i + p_j) \boldsymbol{n}_j W_{ij} S_j, \ \text{if} \ \boldsymbol{r}_{ij} \cdot \boldsymbol{n}_j > 0, \tag{24}$$

Here, F denotes the SPH fluid domain, while the definitions of other symbols remain consistent with those in Eq. (8). Criterion $\boldsymbol{r}_{ij} \cdot \boldsymbol{n}_j > 0$ can ensure that the force calculation on the boundary particles under thin-walled structures only considers particles on the same side, without considering the influence of particles on the other side of thin-walled structures. After obtaining the fluid forces acting on the single-layer particles, the corresponding forces at the center of surface meshes are determined through the mapping relationship between single-layer particles and surface meshes. These forces are then interpolated to the nodes of the surface mesh using shape functions. Since the solid elements share

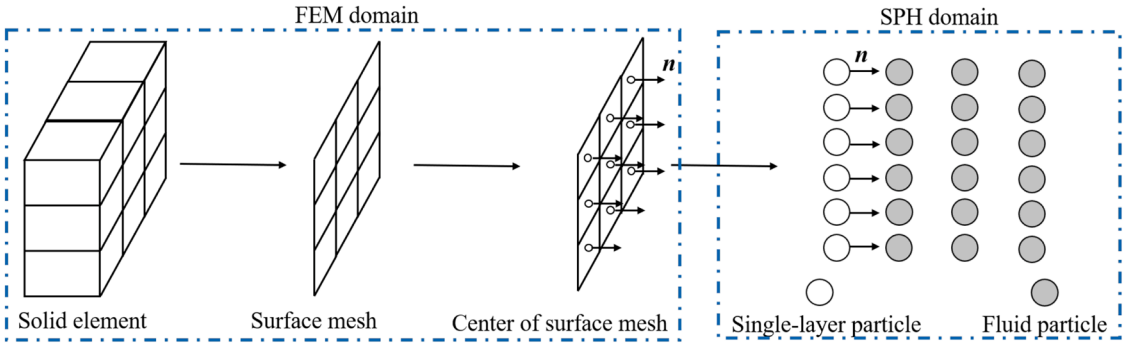


Fig. 4. Coupling interface between SPH domain and FEM elements.

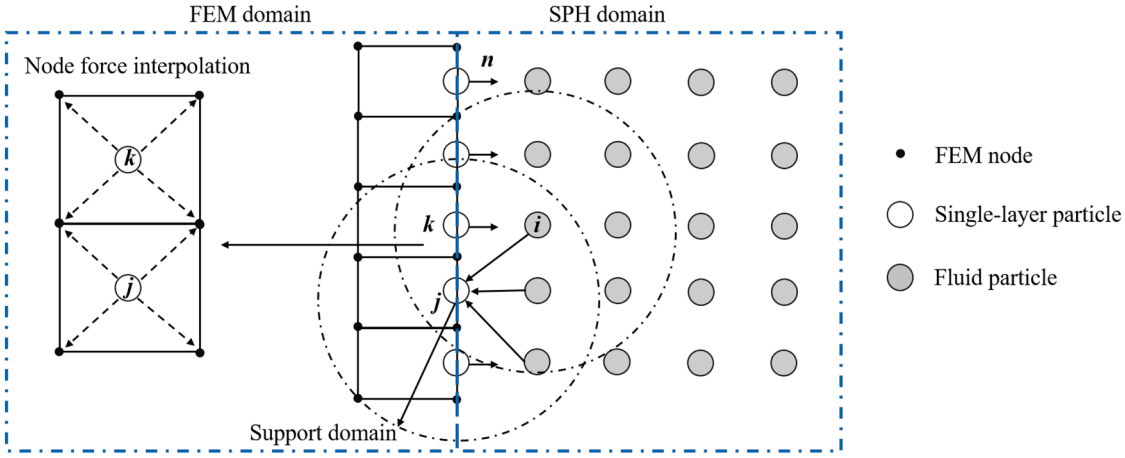


Fig. 5. Data transfer between SPH particles and FEM nodes.

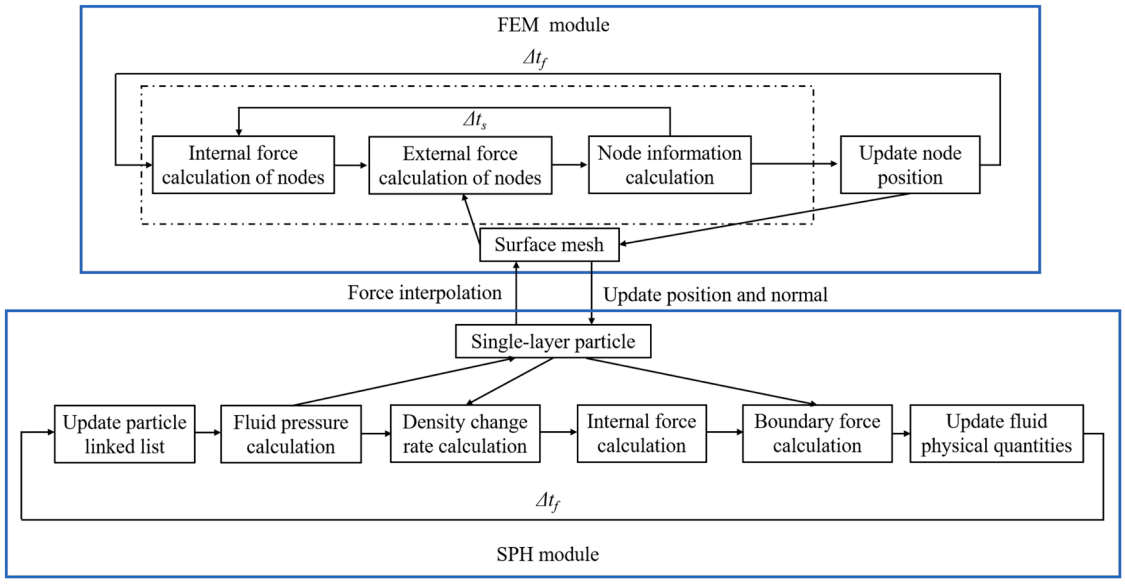


Fig. 6. Computational procedure of the SPH-FEM coupling algorithm.

nodes with surface meshes, the surface loads on the solid elements are thereby obtained, which serve as the external nodal forces in the finite element module computations. The complete computational procedure of the SPH-FEM coupling algorithm is illustrated in Fig. 6.

In Fig. 6, Δt_f represents the time step for the SPH module, determined according to Eq. (10), while Δt_s denotes the time step for the FEM module, obtained from Eq. (23). In this study, both the SPH and FEM modules employ adaptive time step schemes. Typically, the FEM time step Δt_s is smaller than the SPH time step Δt_f. To ensure the stability of coupled computations, Δt_s is modified in Eq. (23) through the following expression:

$$\begin{cases} \Delta t_{cr} = \min_e \frac{l_e}{c_e}, \\ \Delta t_{el} = \alpha \Delta t_{cr}, \\ \Delta t_{fe} = \min(\Delta t_f, \Delta t_{el}), \\ \Delta t_s = \min(\Delta t_{fe}, (t_f + \Delta t_f - t_s)). \end{cases} \tag{25}$$

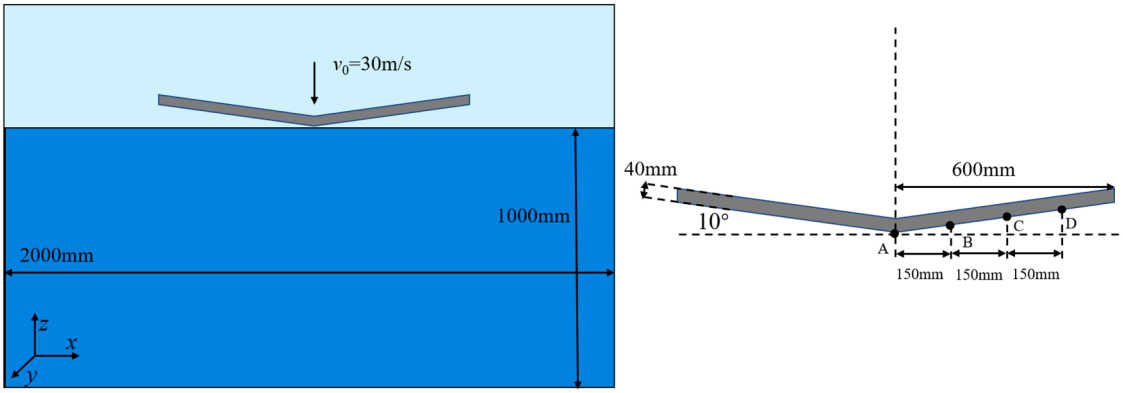


Fig. 7. Geometric sketch of water impact model for an elastic wedge.

Eq. (25) ensures that Δt_s of the FEM module remains smaller than Δt_f of the SPH module, while also preventing the final time step Δt_s in the FEM module from exceeding the computational boundary.

In the SPH-FEM coupling algorithm, during the time step Δt_f, the following procedures are sequentially executed: First, the linked-list update and neighbor particle search are performed in the SPH module to identify interacting particle pairs. The pressure of SPH fluid particles is then computed based on the equation of state, followed by the calculation of density variations and hydrodynamic forces acting on the particles, along with the update of flow field information.

Concurrently, after obtaining the pressure field of SPH particles, the hydrodynamic forces acting on the single-layer particles are calculated via Eq. (24). These forces are subsequently interpolated to the nodes of surface meshes using shape functions, serving as surface loads for the FEM computation and contributing to the nodal force calculations of FEM elements.

3. Benchmark validations

3.1. Numerical simulation of water impact for an elastic wedge

The water impact of an elastic wedge serves as a classical FSI benchmark. Although geometrically simple, its entry process involves complex FSI phenomena, including fluid impact, structural deformation, and dynamic response. Moreover, the existence of semi-analytical solutions and reference results (Khayyer et al., 2018a; Zhang et al., 2022) enables validation of numerical algorithms in terms of accuracy, stability, and convergence when addressing FSI problems. Based on the works of Scolan (2004), Khayyer et al. (2018a) and Zhang et al. (2022), the constant-velocity water impact process of an elastic wedge is simulated to verify the computational accuracy of the proposed SPH-FEM coupling algorithm for solving hydroelastic problems.

3.1.1. Numerical model of water impact for an elastic wedge

The numerical model for the water impact of an elastic wedge in this case is illustrated in Fig. 7. The wedge has a single-side length of 600 mm, a thickness of 40 mm, and a width of 100 mm. In the numerical model, SPH fluid particles are used to construct the water tank, with the fluid domain dimensions being 2000 mm × 100 mm × 1000 mm. The wedge impacts the water surface at a constant velocity of 30 m/s. At the initial computational moment, the bottom of the wedge is tangent to the water surface. Four monitoring points (A, B, C, D) are placed at the quarter points along one side of the wedge to measure the displacement and pressure.

The modeling of solids is primarily divided into two components: the tank walls are constructed using the single-layer particle boundary algorithm, while the wedge is modeled with FEM elements. The body of the wedge is discretized using hexahedral elements, with its surface represented by quadrilateral elements that share nodes with the hexahedral elements. The single-layer particle boundary of rigid walls is composed of triangular elements, mainly based on STL (Standard Triangle Language) files (Guan et al., 2024b).

To ensure the wedge maintains a constant velocity during water entry, the nodes near its symmetry axis are constrained to retain only translational degrees of freedom in the Z-direction, with a fixed velocity of 30 m/s. According to the setting of Khayyer et al. (2018a), the numerical parameters of water impact for an elastic wedge are shown in Table 1, where f represents the fluid domain and s represents the solid domain.

Table 1
The numerical parameters of water impact for an elastic wedge.

Modules	Parameters	Values
SPH	Fluid density ρ_f	1000 kg/m^3
SPH	Sound speed c_0	400 m/s
FEM	Solid density ρ_s	2700 kg/m^3
FEM	Elastic modulus E	67.5 GPa
FEM	Poisson ratio ν	0.33
SPH/FEM	Time t	0.0025 s

3.1.2. Numerical results of water impact for an elastic wedge

Scolan (2004) performed a theoretical analysis of slamming pressure during wedge water entry by integrating the Wagner model, deriving semi-analytical solutions for both the deflection and pressure distribution of the elastic wedge throughout the water impact process. In our study, the semi-analytical and simulation results are adopted as benchmark references.

Before conducting the numerical simulation of water entry, a convergence analysis is carried out to determine the particle resolution within the SPH domain and the mesh resolution in the FEM module. Additionally, the efficacy of the boundary shield algorithm is validated within the context of the SPH-FEM coupling framework.

Three distinct particle/mesh resolution configurations are selected: $\Delta x_f/\Delta x_s = 10\,\text{mm}/10\,\text{mm}$, $\Delta x_f/\Delta x_s = 5\,\text{mm}/10\,\text{mm}$, and $\Delta x_f/\Delta x_s = 5\,\text{mm}/5\,\text{mm}$. Numerical simulations of the wedge water entry process are conducted at different resolutions, from which the deflection history at Point C is extracted. The results are compared with the semi-analytical solutions from Scolan (2004) for validation. The deflection curves at Point C for the various resolution schemes are presented in Fig. 8.

The deflection curves at Point C under three different particle/mesh resolution schemes demonstrate excellent agreement, confirming that the computational results have converged when the resolution is finer than $\Delta x_f/\Delta x_s = 10\,\text{mm}/10\,\text{mm}$. Owing to the short duration of the wedge impact event and the high computational efficiency of the improved SPH-FEM coupling algorithm, the simulation at the $\Delta x_f/\Delta x_s = 5\,\text{mm}/5\,\text{mm}$ resolution requires only

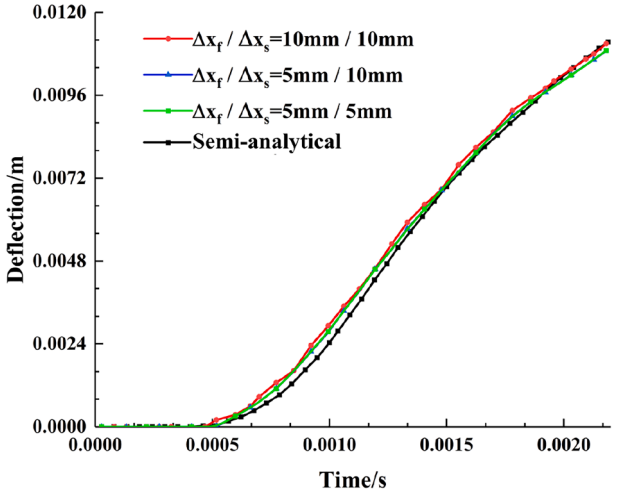


Fig. 8. Comparison of deflection curves between SPH simulation results of different resolutions and reference results (Scolan, 2004).

5 hours. To achieve a more refined fluid-structure interface, the $\Delta x_f/\Delta x_s = 5\,\text{mm}/5\,\text{mm}$ resolution is adopted for all subsequent SPH-FEM simulations of the water impact process.

Simultaneously, the case with a particle/mesh resolution of $\Delta x_f/\Delta x_s = 5\,\text{mm}/10\,\text{mm}$ is selected to analyze the effectiveness of the boundary shield algorithm based on the single-layer particle technique under multi-resolution conditions in this section. A comparative analysis of the simulation results for wedge water entry with and without the application of the boundary shield algorithm is presented in Fig. 9.

At the particle/mesh resolution of $\Delta x_f/\Delta x_s = 5\,\text{mm}/10\,\text{mm}$, the resolution of fluid particles differs from that of solid elements. Without applying the boundary shield algorithm, significant penetration phenomena are observed at the fluid-structure interface. In contrast, the implementation of the boundary shield algorithm effectively suppresses fluid particle penetration at the interface. Under the resolution of $\Delta x_f/\Delta x_s = 5\,\text{mm}/5\,\text{mm}$, where the fluid and solid resolutions are identical, no noticeable particle penetration occurs even without the boundary shield algorithm, and the results are essentially consistent with those obtained using the algorithm.

As detailed in Guan et al. (2024b), the robustness and effectiveness of the boundary shield algorithm based on the single-layer particle technique have been thoroughly demonstrated. The algorithm maintains computational stability in flow field simulations when particles and grids are uniformly distributed, while effectively preventing fluid particle penetration in cases of multi-resolution or non-uniform discretization, thereby ensuring computational robustness. The solver in our study uses the cell-linked list algorithm for neighbor particles, and the increase of boundary particles in the cell does not significantly affect the calculation efficiency, so the size of boundary particles can be smaller than the spacing between fluid particles. At the same time, due to the support domain radius of the kernel function being 2.5 times the spacing between fluid particles, the spacing of boundary particles should not exceed twice that of fluid particles. Therefore, the size of finite element meshes can be smaller than the spacing between fluid particles, but up to twice the spacing between fluid particles.

Consequently, the boundary shield algorithm is uniformly applied in all subsequent SPH-FEM simulations.

Upon completion of the simulation for the water entry, the pressure data from monitoring points A, C, and D are extracted. Khayyer et al. (2018a) and Zhang et al. (2022) also conducted numerical simulations of the water impact process for a wedge and obtained a series of numerical results with the ISPH (Incompressible SPH)-SPH and MPS-FEM model. The comparison between simulation results and reference results is presented in Fig. 10. The pressure curves obtained through the SPH-FEM coupling algorithm show agreement with the reference results, particularly at the pressure peaks, which can validate the computational accuracy of the proposed algorithm for solving FSI problems involving elastic structures. However, certain discrepancies exist between SPH-FEM simulation results and the semi-analytical solution. It is noted that the MPS-FEM and ISPH-SPH results also show certain discrepancies from the semi-analytical solution. The semi-analytical solution is derived under the assumption of incompressible fluid, whereas actual numerical simulations inherently involve pressure fluctuations and numerical oscillations, leading to the observed discrepancies.

Then, the pressure and stress contours of Khayyer et al. (2018a) are selected as reference data for comparison. The simulation results obtained through the proposed SPH-FEM coupling algorithm in our study are compared with the ISPH-SPH simulation results in Fig. 11.

In the SPH-FEM simulation results of this case, the fluid particles are visualized using pressure contours, while the solid elements are represented by contours of the stress component σ_{xx}. Both the fluid pressure field and the wedge stress field remain stable throughout the simulation process. Compared to the simulation results of Khayyer et al. (2018a), the pressure distribution at the fluid-structure interface in this study appears less smooth. This phenomenon is attributed to pressure oscillations caused by non-uniform particle distribution during the mesh-to-particle conversion process. However, the oscillations do not adversely affect the overall computation of the flow field or the stress field calculation of the wedge.

Notably, the pressure and stress contours obtained from the SPH-FEM coupling algorithm demonstrate excellent agreement with the ISPH-SPH simulation results during water impact, particularly at the moment of slamming, which can validate the computational accuracy of the improved SPH-FEM coupling algorithm proposed in our study for simulating water entry problems of elastic structures.

3.2. Numerical simulation for impact of dam-break flow on an elastic baffle

Dam-break flow impacting an elastic baffle represents a classic FSI problem involving elastic bodies, which serves as a benchmark case widely adopted for validating the computational accuracy of numerical algorithms in FSI simulations. Based on the work of Shi et al. (2024), the same condition for the impact of dam-break flow on an elastic baffle is selected to validate the computational accuracy of the improved SPH-FEM coupling algorithm proposed in this study.

3.2.1. Numerical model for impact of dam-break flow on an elastic baffle

The numerical model for the impact of dam-break flow on an elastic baffle is illustrated in Fig. 12. The simulation scenario is configured within an enclosed tank with dimensions of $584\,\text{mm} \times 80\,\text{mm} \times 365\,\text{mm}$. The fluid domain is initially positioned on the left side of the tank, with dimensions of $146\,\text{mm} \times 80\,\text{mm} \times 292\,\text{mm}$, representing the initial state of the dam-break flow. An elastic baffle with dimensions of $12\,\text{mm} \times 80\,\text{mm} \times 80\,\text{mm}$ is placed $292\,\text{mm}$ from the left side of the tank. Point P is located at the midpoint of the top edge of the elastic baffle.

In the numerical simulation, SPH fluid particles are employed to model the dam-break flow, while the tank walls are constructed using the single-layer particle boundary algorithm. The elastic baffle is discretized with finite elements, where its main body is meshed with hexahedral elements and its surface is represented by quadrilateral elements that share nodes with the hexahedral elements. All degrees of freedom of the nodes on the bottom surface of the elastic baffle are constrained to zero, maintaining a fixed connection with the tank bottom. According to the setting of Shi et al. (2024), the numerical parameters of dam-break flow impact on an elastic baffle are shown in Table 2.

3.2.2. Numerical results for impact of dam-break flow on an elastic baffle

Prior to conducting the numerical simulation of dam-break flow impacting an elastic baffle, a convergence analysis must first be performed

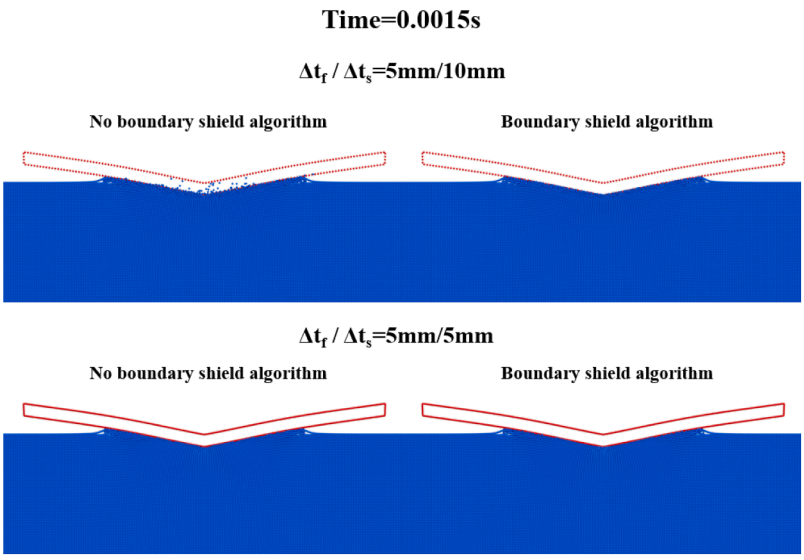


Fig. 9. Comparison of fluid-structure interface under different resolutions and boundary shield algorithms.

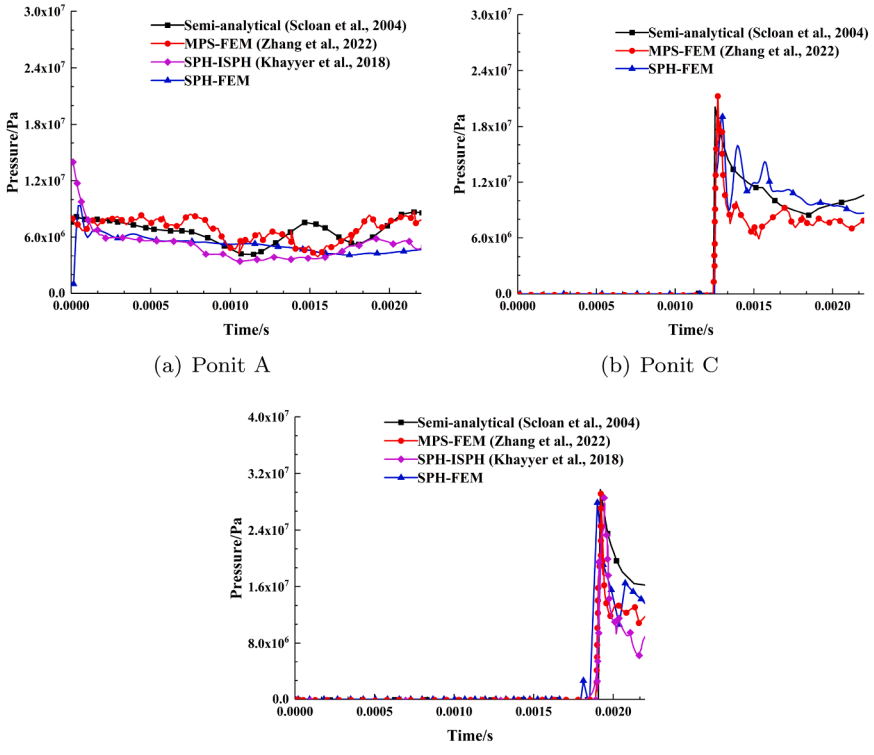


Fig. 10. Comparison of pressure curves at different measuring points between simulation results and reference results (Scolan, 2004; Khayyer et al., 2018a; Zhang et al., 2022) during the water impact process of an elastic wedge.

Table 2
The numerical parameter of dam-break flow impact on an elastic baffle.

Modules	Parameters	Values
SPH	Fluid density ρ_f	1000 kg/m^3
SPH	Sound speed c_0	30 m/s
FEM	Solid density ρ_s	2500 kg/m^3
FEM	Elastic modulus E	1 MPa
FEM	Poisson ratio ν	0
SPH/FEM	Time t	1 s

on the particle resolution of the SPH computational domain and the mesh resolution of the FEM module. Three distinct particle/mesh resolution configurations are selected: $\Delta x_f/\Delta x_s = 5\,\text{mm}/3\,\text{mm}$, $\Delta x_f/\Delta x_s = 3\,\text{mm}/2\,\text{mm}$, and $\Delta x_f/\Delta x_s = 2\,\text{mm}/2\,\text{mm}$. Numerical simulations for the impact of dam-break flow on an elastic baffle are conducted at different resolutions, and the lateral displacement at Point P is extracted for comparative validation. The displacement curves at Point P for the various resolution schemes are presented in Fig. 13.

When the particle/mesh resolution is finer than $\Delta x_f/\Delta x_s = 3\,\text{mm}/2\,\text{mm}$, the displacement curve at Point P begins to demonstrate convergence. At the resolution of $\Delta x_f/\Delta x_s = 2\,\text{mm}/2\,\text{mm}$, the improved

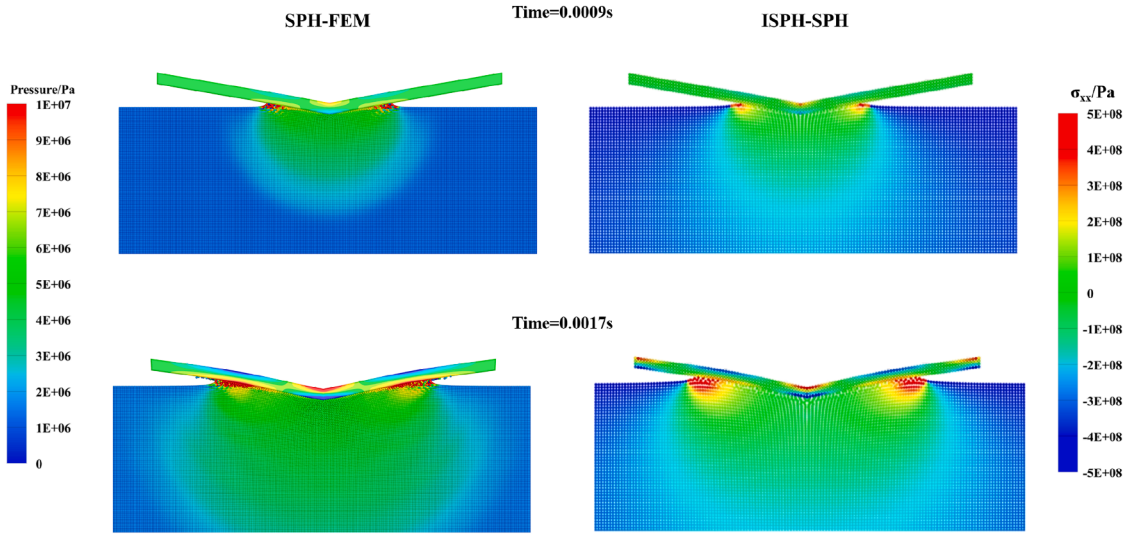


Fig. 11. Comparison of pressure and stress contours between SPH-FEM results (left) and reference results (Khayyer et al., 2018a) (right) for the water entry process.

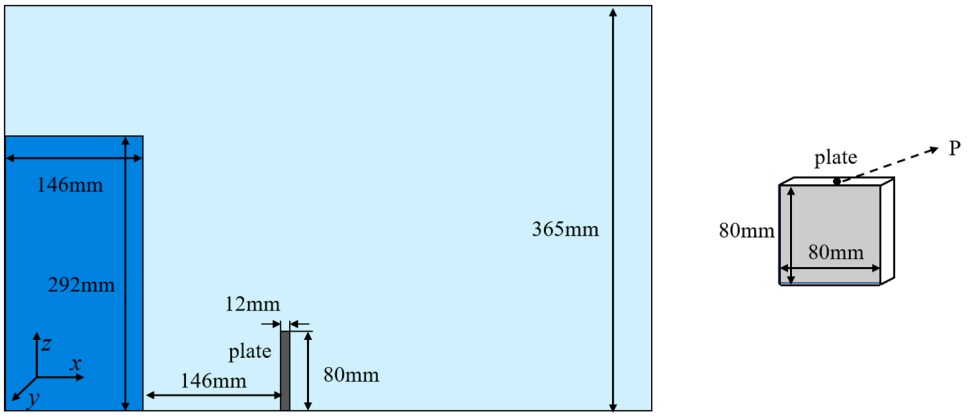


Fig. 12. Geometric sketch for impact of dam-break flow on an elastic baffle.

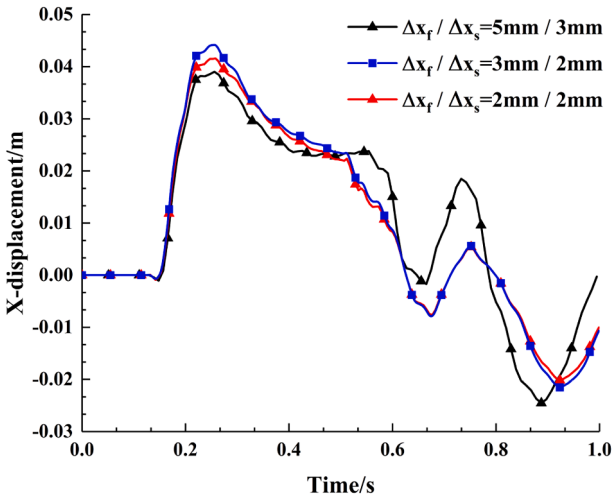


Fig. 13. Comparison of displacement curves of SPH-FEM results with different resolutions.

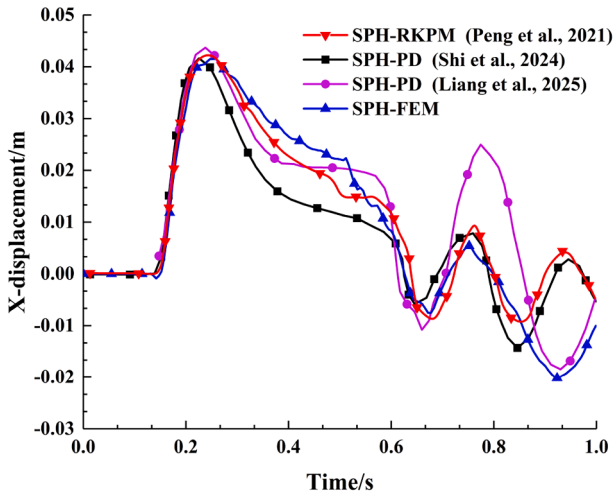


Fig. 14. Comparison of displacement curves between SPH-FEM results and reference results (Shi et al., 2024; Peng et al., 2021; Liang et al., 2025).

SPH-FEM coupling model requires only 24 hours to simulate 1 second of physical time for the impact of dam-break flow on an elastic baffle. To achieve a more refined fluid-structure interface, the $\Delta x_f/\Delta x_s$ = 2 mm/2 mm resolution is adopted for all subsequent SPH-FEM coupling numerical simulations.

Peng et al. (2021) conducted numerical simulations for the impact of dam-break flow on an elastic baffle with the same parameters using a coupled SPH-RKPM (Reproduction Kernel Particle Method) model, obtaining a series of numerical results. Shi et al. (2024) and Liang et al. (2025) adopted a coupled SPH and Peridynamics (PD) model to conduct

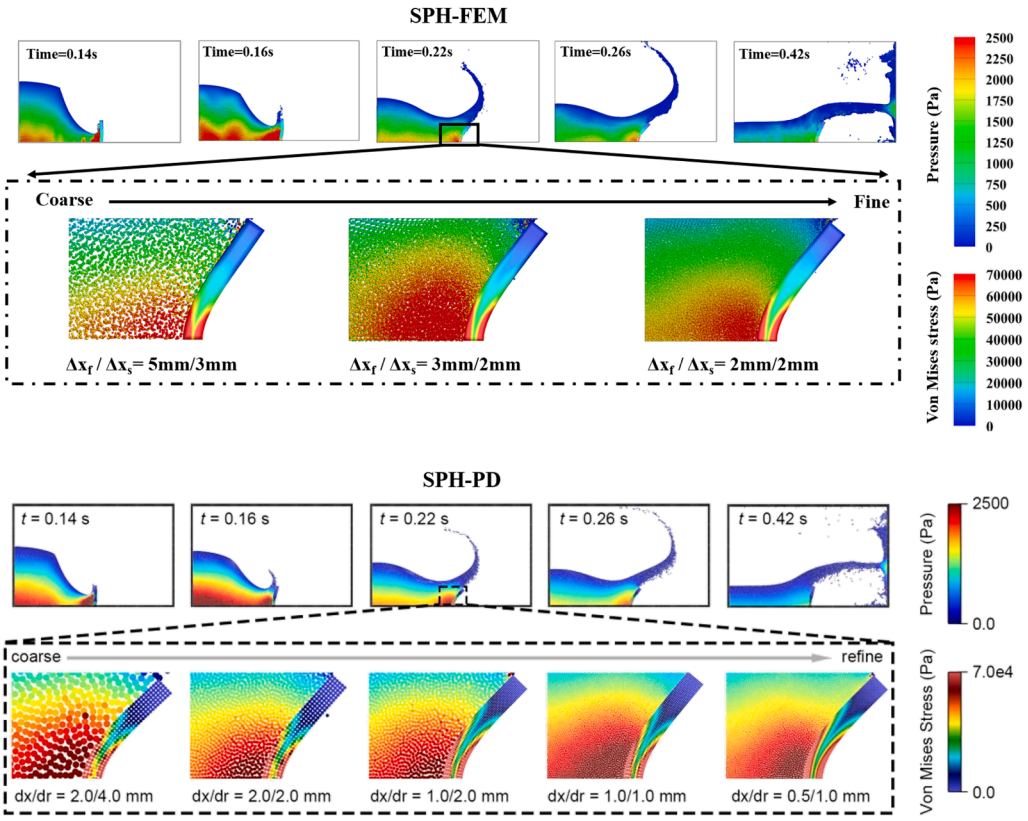


Fig. 15. Comparison of pressure and stress contours between SPH-FEM results (top) and reference results (bottom) (Shi et al., 2024) for dam-break flow impact on an elastic baffle.

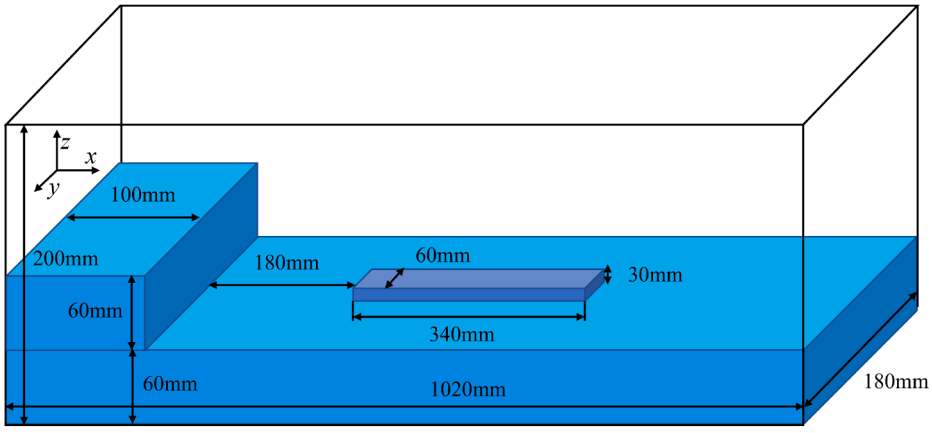


Fig. 16. Geometric sketch of flexible floating body under dam-break flow impact.

the same numerical simulations. Therefore, their simulation results are selected as reference data for comparison. The computational results for the displacement at Point P of the baffle obtained through the proposed SPH-FEM coupling model in this study are compared with the reference results, as shown in Fig. 14. These models demonstrate consistent peak values and variation trends in the lateral displacement of the baffle, validating the computational accuracy of the SPH-FEM coupling model proposed in this paper for handling FSI problems involving elastic bodies. However, due to differences in the boundary reflection conditions and damping, some discrepancies are observed in the later phase of the oscillation curves between the simulation results.

Simultaneously, the simulation results for the impact of dam-break flow on an elastic baffle at different instances are extracted. The fluid particles are visualized using pressure contours, while the solid elements are represented by Von Mises stress contours. Throughout the simulation, both the fluid pressure field and the solid stress field remain stable. The results are compared with the simulation outcomes from Shi et al. (2024), as shown in Fig. 15.

Based on the displacement curve of Point P and the contour plots, it can be observed that during the initial stage of the dam-break flow impacting the elastic baffle, the fluid domain begins to break up and form the dam-break flow. At 0.14 s, the dam-break flow reaches the elastic baffle. While the bottom of the baffle remains fixed, its main body starts moving rightward. By 0.22 s, the lateral displacement of the elastic baffle reaches its maximum value, accompanied by maximal bending deformation. Simultaneously, the Von Mises stress at the bottom of the

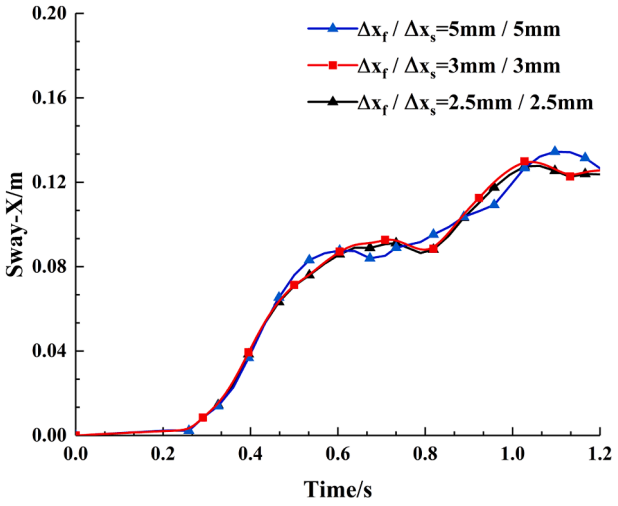


Fig. 17. Comparison of sway displacement curves of SPH-FEM results with different resolutions.

baffle reaches its maximum value. After 0.22 s, the elastic baffle begins to return toward its original position. At 0.62 s, it completely returns to its initial position and starts moving leftward. Subsequently, the baffle enters an oscillatory state.

According to Fig. 15, the Von Mises stress contours of the elastic baffle obtained through the SPH-FEM coupling algorithm show excellent agreement with the simulation results from the SPH-PD coupling algorithm. Furthermore, the deformation state of the elastic baffle and the fluid splash morphology are also highly consistent, demonstrating the computational accuracy of the proposed SPH-FEM coupling algorithm in handling FSI problems involving elastic bodies.

It should be noted that the stress contours in the SPH-PD simulation results from the reference (Shi et al., 2024) employed a customized colorbar, where the red region representing higher stress values is broadly distributed. The colorbar difference stems from the different visualization software: ParaView for the reference and Tecplot for our simulation results. Each software applies its own native color mapping scheme, hence the visual discrepancy. These differences are solely attributable to post-processing techniques rather than computational inconsistencies.

Additionally, the Von Mises stress distributions obtained with the SPH-FEM coupling algorithm at resolutions of $\Delta x_f/\Delta x_s = 3\,\text{mm}/2\,\text{mm}$ and $\Delta x_f/\Delta x_s = 2\,\text{mm}/2\,\text{mm}$ achieve computational accuracy comparable to that of the SPH-PD algorithm at resolutions of $\Delta x_f/\Delta x_s = 1\,\text{mm}/2\,\text{mm}$ and even $\Delta x_f/\Delta x_s = 0.5\,\text{mm}/1\,\text{mm}$. The results confirm that the proposed SPH-FEM coupling algorithm exhibits superior robustness and higher computational efficiency.

3.3. Numerical results of flexible floating body under dam-break flow impact

The free motion response of flexible floating bodies under water impact represents a common FSI problem in naval architecture and ocean engineering. When such structures are subjected to fluid loads from waves in marine environments, they exhibit complex motion responses and structural deformations. Based on the work of Zhang et al. (2022), the case of a flexible floating body under dam-break flow impact is simulated to validate the computational accuracy of the improved SPH-FEM coupling algorithm proposed in this paper.

3.4. Numerical model of flexible floating body under dam-break flow impact

The numerical model for the flexible floating body under dam-break flow impact in this case study is illustrated in Fig. 16. The scenario involves a semi-enclosed tank with dimensions of 1020 mm × 180 mm × 200 mm. The fluid computational domain consists of two parts: one situated at the bottom of the tank with dimensions of 1020 mm × 180 mm × 60 mm, and another located on the left side of the tank, representing the initial state of the dam-break flow, with dimensions of 100 mm × 180 mm × 60 mm.

Table 3
The numerical parameters of flexible floating body under dam-break flow impact.

Modules	Parameters	Values
SPH	Fluid density ρ_f	1000 kg/m^3
SPH	Sound speed c_0	30 m/s
FEM	Solid density ρ_s	625 kg/m^3
FEM	Elastic modulus E	0.1/10 MPa
FEM	Poisson ratio ν	0.3
SPH/FEM	Time t	1.2 s

A flexible floating body is positioned 280 mm from the left side of the tank. The body has a rectangular shape with dimensions of 340 mm × 60 mm × 30 mm, and is centered along the Y-direction of the tank. The floating body is in a state of buoyancy-gravity equilibrium. The density of the flexible floating body is 625 kg/m^3, resulting in an immersed depth of 18.75 mm.

In the SPH-FEM simulation, the tank walls are modeled using the single-layer particle boundary algorithm, while the flexible floating body, being a solid structure, is discretized with hexahedral elements for its main body and quadrilateral elements sharing nodes with the hexahedral elements for its surface. All nodal degrees of freedom of the floating body are unconstrained. According to the setting of Zhang et al. (2022), the numerical parameters of flexible floating body under dam-break flow impact are shown in Table 3.

Prior to conducting the numerical simulation of the flexible floating body motion under dam-break flow impact, a convergence analysis is first performed for the case with elastic modulus $E = 10\,\text{MPa}$ to evaluate the particle resolution of the SPH computational domain and the mesh resolution of the FEM module. Three distinct particle/mesh resolution configurations are selected: $\Delta x_f/\Delta x_s = 5\,\text{mm}/5\,\text{mm}$, $\Delta x_f/\Delta x_s = 3\,\text{mm}/3\,\text{mm}$, and $\Delta x_f/\Delta x_s = 2.5\,\text{mm}/2.5\,\text{mm}$. Numerical simulations of the flexible floating body motion under dam-break flow impact are carried out at different resolutions. The sway displacement of the flexible floating body is extracted for comparative validation, and the sway displacement curves for the various resolution schemes are presented in Fig. 17.

When the particle/mesh resolution is finer than $\Delta x_f/\Delta x_s = 3\,\text{mm}/3\,\text{mm}$, the sway displacement curve of the flexible floating body begins to demonstrate convergence. Therefore, to balance computational efficiency and accuracy, the particle/mesh resolution of $\Delta x_f/\Delta x_s = 3\,\text{mm}/3\,\text{mm}$ is selected for subsequent SPH-FEM simulations of the flexible floating body motion under dam-break flow impact.

Zhang et al. (2022) conducted numerical simulations of the flexible floating body motion under dam-break flow impact using the coupled MPS-FEM algorithm, obtaining a series of numerical results. Therefore, their simulation results are selected as reference data for comparison. The computational results of the sway and surge displacement curves for a flexible floating body with different elastic modulus ($E = 0.1\,\text{MPa}$ and $E = 10\,\text{MPa}$) obtained by the proposed SPH-FEM algorithm in this study are compared with those from the MPS-FEM algorithm in Fig. 18.

The results from both algorithms show consistent sway and surge displacements across different elastic modulus, validating the computational accuracy of the improved SPH-FEM coupling algorithm proposed in this paper for handling FSI problems involving elastic bodies. Furthermore, the sway and surge displacements of the flexible floating body with elastic modulus $E = 0.1\,\text{MPa}$ are significantly more pronounced, demonstrating that the elastic modulus substantially influences the motion response of flexible floating bodies.

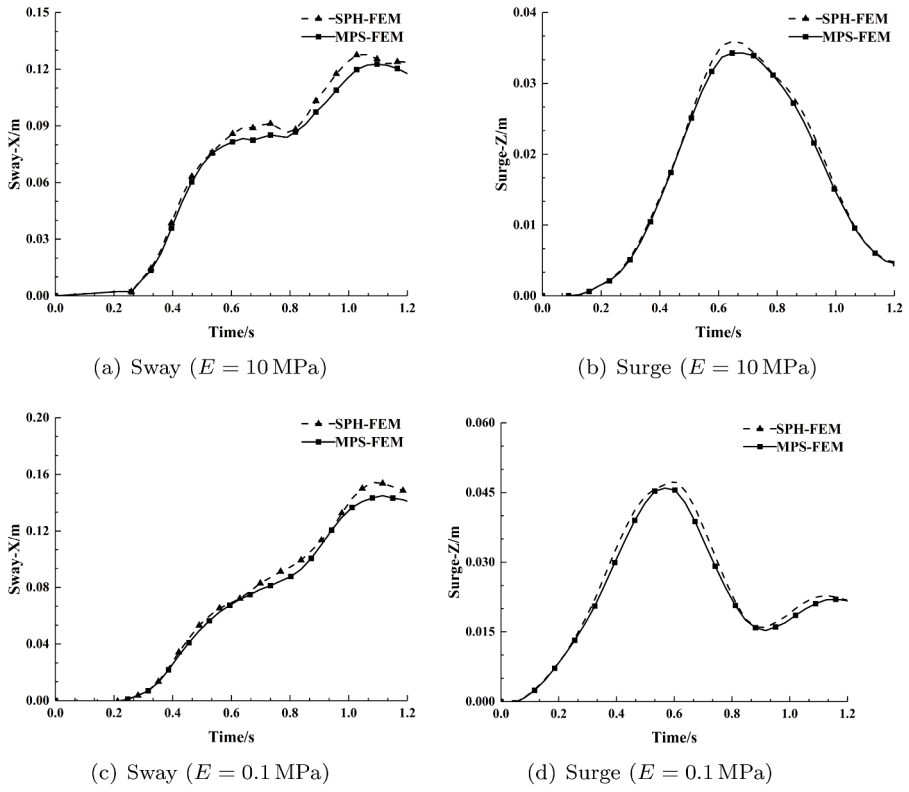


Fig. 18. Comparison of sway and surge displacement curves between SPH-FEM results and reference results (Zhang et al., 2022) for an flexible floating body under dam-break flow impact.

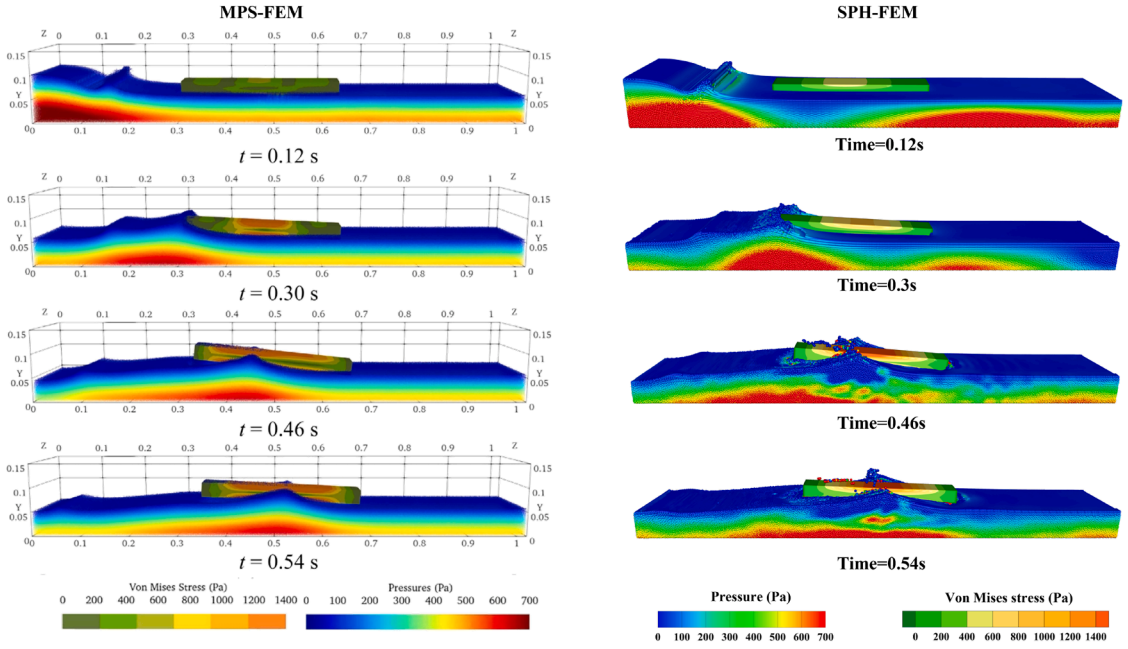


Fig. 19. Comparison of pressure and stress contours between SPH-FEM results (right) and reference results (left) (Zhang et al., 2022) for an flexible floating body under dam-break flow impact with $E = 10$ MPa.

The pressure and stress contour plots during the motion of the flexible floating body under different elastic modulus are extracted for comparison with reference results from Zhang et al. (2022), as shown in Figs. 19 and 20. Fluid particles are visualized using pressure contours, while solid elements are represented by Von Mises stress contours.

During the motion of the flexible floating body, the dam-break flow initially fractures and generates rightward propagating waves at the beginning of the simulation. At 0.3 s, the wave impacts the flexible floating body, causing deformation. By 0.54 s, the wave reaches the mid-section of the floating body and lifts it upward. At this moment, the bending deformation of the flexible floating body reaches its maximum, and the Von Mises stress correspondingly peaks. Subsequently, the wave arrives at the stern of the floating body by 0.78 s, and finally reaches the right-side wall at 1.12 s, completing one oscillation cycle of the floating body. The complete deformation of the flexible floating body with elastic mod-

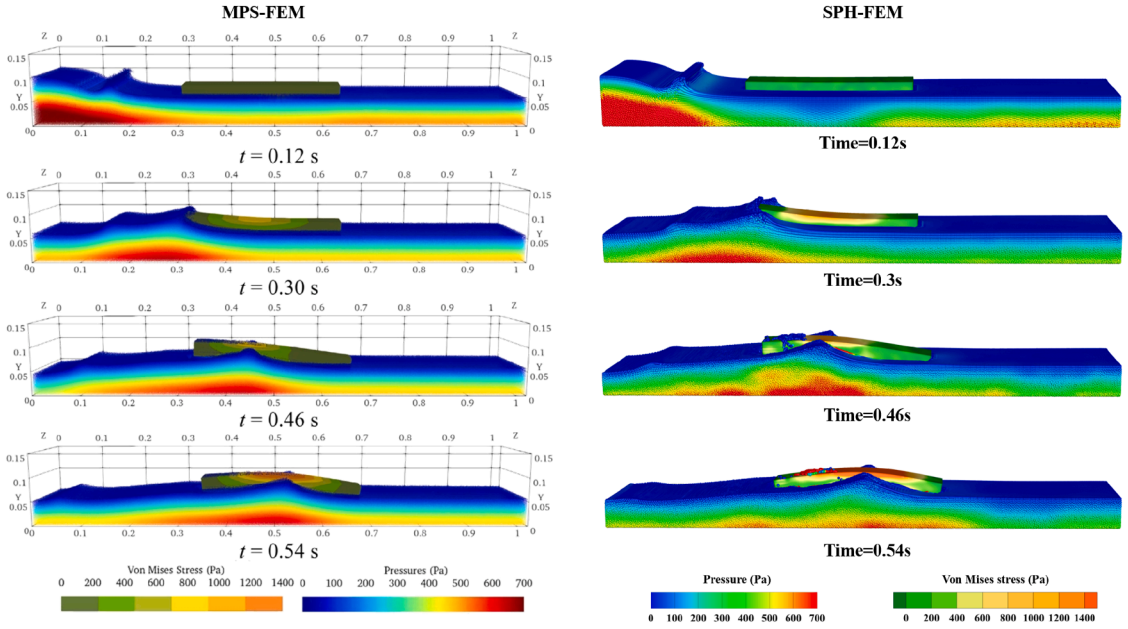


Fig. 20. Comparison of pressure and stress contours between SPH-FEM results (right) and reference results (left) (Zhang et al., 2022) for an flexible floating body under dam-break flow impact with $E = 0.1$ MPa.

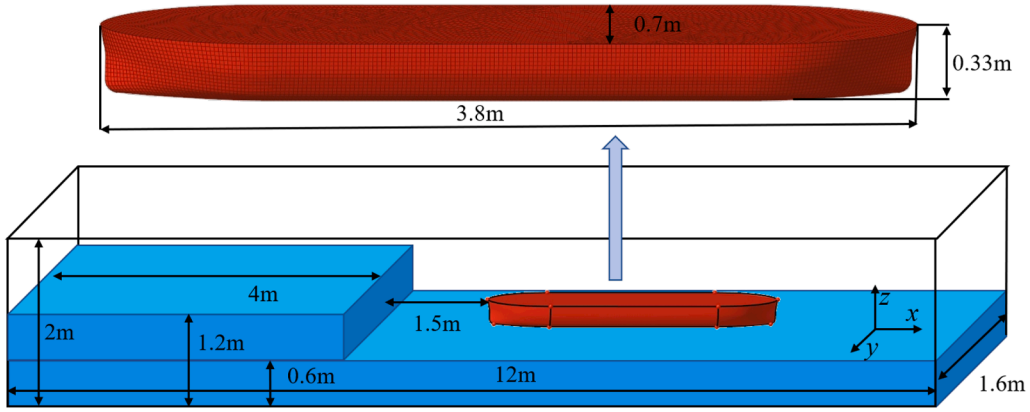


Fig. 21. Numerical model of wave impact on an elastic ship.

ulus $E = 0.1$ MPa is significantly larger than that with $E = 10$ MPa, particularly at 0.54 s.

Since the colorbar definitions differ between the SPH-FEM and MPS-FEM simulation results, the visualized Von Mises stress exhibits apparent discrepancies, although the actual simulated values are in good agreement. In the SPH-FEM simulation with elastic modulus $E = 0.1$ MPa, some fluid particles splash onto and accumulate on the left side of the top surface during the dam-break impact. Due to the relatively low elastic modulus of the floating body, the bending deformation at its left end at 0.3 s is more pronounced compared to the reference results.

Despite these minor differences, the pressure and stress contours during the motion of the flexible floating body for both elastic modulus ($E = 0.1$ MPa and $E = 10$ MPa) show excellent agreement with the MPS-FEM simulation results from Zhang et al. (2022). The consistency validates the computational accuracy of the improved SPH-FEM coupling algorithm proposed in this paper for addressing FSI problems involving flexible floating bodies.

4. Numerical simulation of wave impact on an elastic ship

In the benchmark cases presented in this paper, although the simulation results based on the improved SPH-FEM coupling algorithm show good agreement with reference solutions, the elastic boundaries in these benchmarks are relatively simple and feature regular geometric shapes. The section extends the simulation to the deformation and motion response of an elastic ship under wave impact. The elastic ship possesses complex curved surfaces, thereby validating the feasibility of the improved SPH-FEM coupling algorithm proposed in this paper for handling FSI problems involving complex elastic boundaries.

4.1. Numerical model of wave impact on an elastic ship

Buchner (2002) has demonstrated the feasibility of generating waves through dam-break flows. Therefore, the wave in this case is generated via a dam-break process. The numerical model for wave impact on the elastic ship is illustrated in Fig. 21. The numerical water tank has dimensions of 12 m × 1.6 m × 2 m. The fluid computational domain consists of two parts: one located at the bottom of the tank with dimensions of 12 m × 1.6 m × 0.6 m, and another on the left side of the tank, representing the initial state of the dam-break flow, with dimensions of 4 m × 1.6 m × 0.6 m.

An elastic ship is positioned 5.5 m from the left side of the tank. The principal dimensions of the ship are 3.8 m × 0.7 m × 0.33 m. It is centered along the Y-direction of the tank, with its bottom tangent to the wa-

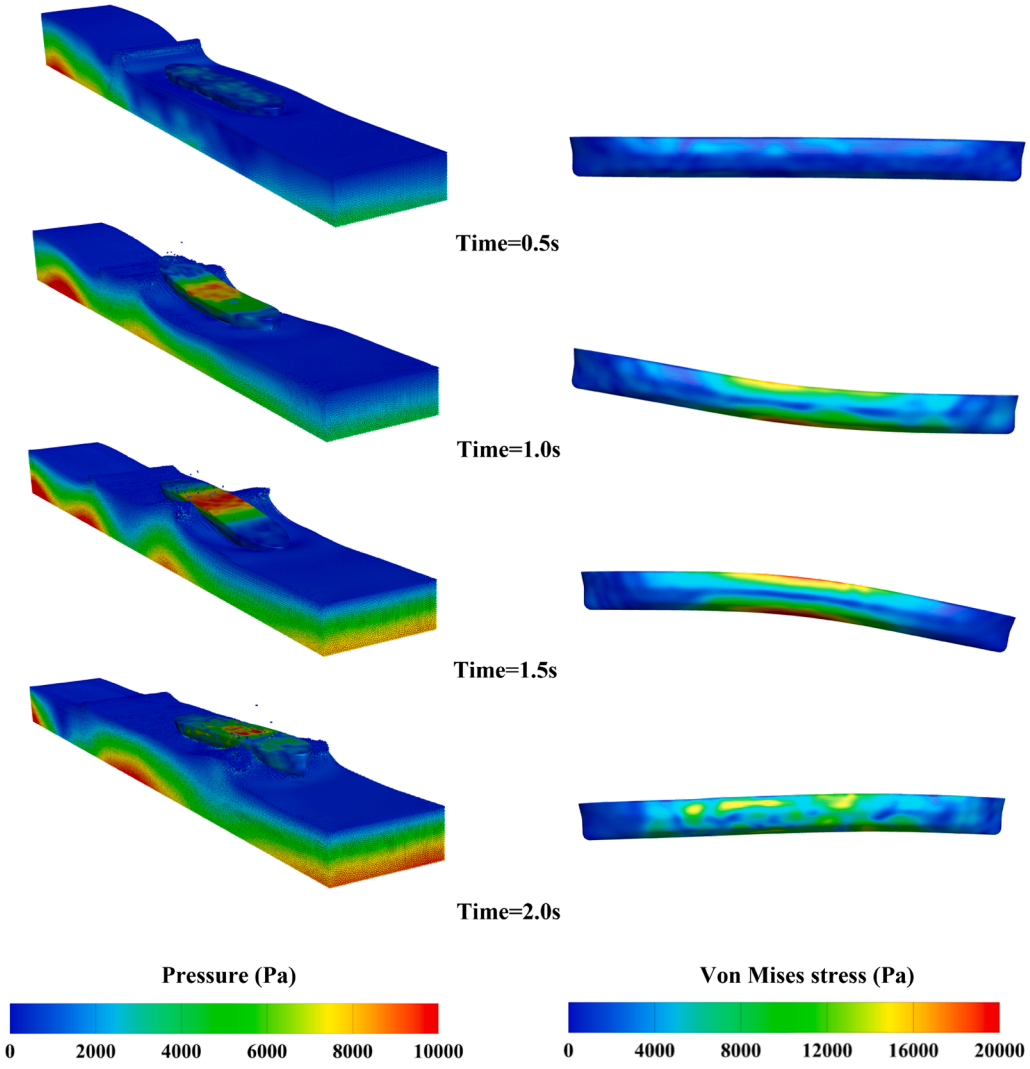


Fig. 22. Pressure and stress contours of SPH-FEM simulation results for an elastic ship under wave impact.

Table 4
The numerical parameters of wave impact on an elastic ship.

Modules	Parameters	Values
SPH	Fluid density ρ_f	1000 kg/m^3
SPH	Sound speed c_0	50 m/s
FEM	Solid density ρ_s	500 kg/m^3
FEM	Elastic modulus E	1 MPa
FEM	Poisson ratio ν	0.3
SPH/FEM	Time t	3 s

ter surface. The detailed numerical model parameters are provided in Fig. 21. According to the setting of Zhang et al. (2022), the numerical parameters of wave impact on an elastic ship are shown in Table 4.

4.2. Simulation result of wave impact on an elastic ship

The wave impact scenario on the elastic ship is similar to the isolated wave impact on a flexible ship hull described in Zhang et al. (2022), which used a particle/mesh resolution of $\Delta x_f/\Delta x_s = 25\,\text{mm}/25\,\text{mm}$. The simulation results in Zhang et al. (2022) are stable, so the particle/mesh resolution of $\Delta x_f/\Delta x_s = 25\,\text{mm}/25\,\text{mm}$ is enough. To demonstrate the computational efficiency of the proposed improved SPH-FEM coupling algorithm, the higher-resolution particle and mesh sizes are selected, which are specifically $\Delta x_f/\Delta x_s = 20\,\text{mm}/20\,\text{mm}$. Due to the relatively complex geometry of the ship, it is difficult to use grids of the same size for discretization. Therefore, the grid size of the ship varies from 0.5 mm to 2 mm according to the complexity of the surface, with a maximum grid size of 2 mm. The configuration includes 1,920,000 fluid particles, 140,540 finite element hexahedral elements, and 192,520 single-layer particles for solid wall boundaries.

The total computation time for simulating the wave impact process on the elastic ship is 24 hours using an OpenMP-based 4-core CPU processor (AMD Ryzen-5-5600). The detailed time distribution for each module is as follows: SPH module accounts for approximately 80% of the total time (about 19.2 hours). FEM module accounts for approximately 20% of the total time (about 4.8 hours).

Since the specific geometric configuration of the elastic ship in this case does not exactly match that in Zhang et al. (2022), our study primarily presents the results obtained with the improved SPH-FEM coupling algorithm. Pressure and stress contours during the wave impact process, along with deformation results of the elastic ship, are extracted and shown in Fig. 22.

In Fig. 22, fluid particles are visualized using pressure contours, while solid elements are represented by Von Mises stress contours. During the wave impact process on the elastic ship, the ship begins to sink at the initial stage. The dam-break flow fractures and generates rightward

propagating waves, which impact the elastic ship and induce deformation. By 1.5 s, the wave reaches the midsection of the ship, at which point the bending deformation of the elastic ship reaches its maximum and the Von Mises stress correspondingly peaks. At 2.0 s, the wave arrives at the stern, and the bending deformation of the elastic ship begins to recover.

During the deformation and motion of the elastic ship under wave impact, despite its complex geometry, both the pressure distribution in the fluid field and the stress distribution in the elastic ship remain stable throughout the FSI process. The stability demonstrates the feasibility of the improved SPH-FEM coupling algorithm proposed in this paper for simulating FSI problems involving complex elastic boundaries.

5. Conclusions and prospects

This paper presents an improved SPH-FEM coupling model based on the single-layer particle boundary algorithm, achieving efficient three-dimensional coupling between fluid particles and solid elements. The algorithm utilizes the FEM surface mesh as an information exchange interface, leveraging both the shared-node characteristics between the FEM surface mesh and hexahedral elements, and the mapping relationship between the surface mesh and the SPH single-layer particle. By eliminating the need for additional node or particle arrangements at the fluid-structure interface typically required in traditional SPH-FEM methods, the improved algorithm enhances information exchange efficiency during coupled computations.

The proposed SPH-FEM coupling model introduces a boundary shield algorithm, which enables the use of different particle and mesh resolutions at the fluid-structure interface. The validation results from benchmark cases demonstrate that the improved SPH-FEM coupling algorithm can effectively simulate various FSI problems involving elastic structures and solve full-scale three-dimensional FSI problems with complex geometries in hydrodynamic scenarios.

Currently, structural discretization in the SPH-FEM coupling model primarily relies on hexahedral elements, which present limitations for modeling complex geometries. Besides, the algorithm is specifically designed for FSI in hydrodynamic scenarios, where the fluid is limited to liquids and the solid primarily to elastic bodies. In future research, we plan to develop an enhanced SPH-FEM coupling framework that incorporates tetrahedral elements, shell elements, beam elements and other fluid constitutive models for a wider range of scenarios.

CRediT authorship contribution statement

Xiang-Shan Guan: Writing – original draft, Visualization, Validation, Software, Resources, Methodology, Investigation, Formal analysis; **Peng-Nan Sun:** Writing – review & editing, Software, Resources, Project administration, Methodology, Funding acquisition, Data curation, Conceptualization; **Xiong Zhang:** Writing – review & editing, Software, Methodology, Funding acquisition, Data curation; **Xin-Yun Ni:** Software, Funding acquisition; **Chun-Mei Xie:** Software, Funding acquisition.

Declaration of competing interest

No conflict of interest exists in the submission of this manuscript, and the manuscript is approved by all authors for publication. We would like to declare that the work described was original research that has not been published previously, and not under consideration for publication elsewhere, in whole or in part. All the authors listed have approved the enclosed manuscript.

Acknowledgments

This research is supported by the National Key Research and Development Program of China (Grant No. 2022YFC2806300); the National Natural Science Foundation of China (Grant Nos. 12472204 and 52401346) and the development and application project of ship CAE software.

References

Antuono, M., Colagrossi, A., Marrone, S., 2012. Numerical diffusive terms in weakly-compressible SPH schemes. Comput. Phys. Commun. 183 (12), 2570–2580.
Antuono, M., Colagrossi, A., Marrone, S., Lugni, C., 2011. Propagation of gravity waves through an SPH scheme with numerical diffusive terms. Comput. Phys. Commun. 182 (4), 866–877.
Antuono, M., Colagrossi, A., Marrone, S., Molteni, D., 2010. Free-surface flows solved by means of SPH schemes with numerical diffusive terms. Comput. Phys. Commun. 181 (3), 532–549.
Barth, T., Herbin, R., Ohlberger, M., 2018. Finite volume methods: foundation and analysis. Encycl. Comput. Mech. Second Edit. , 1–60.
Basting, S., Quaini, A., Čanić, S., Glowinski, R., 2017. Extended ALE method for fluid–structure interaction problems with large structural displacements. J. Comput. Phys. 331, 312–336.
Bathe, K.-J., 2007. Finite element method. Wiley Encyclop. Comput. Sci. Eng. , 1–12.
Buchner, B., 2002. Green water on ship-type offshore structures. Ph.D. thesis. Delft University of Technology Delft, The Netherlands.
Caleyron, F., Combescure, A., Faucher, V., Potapov, S., 2013. Sph modeling of fluid–solid interaction for dynamic failure analysis of fluid-filled thin shells. J. Fluids Struct. 39, 126–153.
Cercos-Pita, J.L., 2015. Aquagpusph, a new free 3d sph solver accelerated with opencl. Comput. Phys. Commun. 192, 295–312.
Chen, C., Shi, W.-K., Shen, Y.-M., Chen, J.-Q., Zhang, A.-M., 2022. A multi-resolution SPH-FEM method for fluid–structure interactions. Comput. Methods Appl. Mech. Eng. 401, 115659.
Chen, C., Zhang, A.-M., Chen, J.-Q., Shen, Y.-M., 2021. Sph simulations of water entry problems using an improved boundary treatment. Ocean Eng. 238, 109679.
Chen, X., Cui, J., Li, J.-Y., Shi, P.-C., 2025. A hydroelastic fluid-structure interaction solver based on a coupled 3d SPH-FEM method. J. Fluids Struct. 137, 104366.
Crespo, A. J.C., Domínguez, J.M., Rogers, B.D., Gómez-Gesteira, M., Longshaw, S., Canelas, R., Vacondio, R., Barreiro, A., García-Feal, O., 2015. DualSPHysics: open-source parallel CFD solver based on smoothed particle hydrodynamics (SPH). Comput. Phys. Commun. 187, 204–216.
De Vuyst, T., Vignjevic, R., Campbell, J.C., 2005. Coupling between meshless and finite element methods. Int. J. Impact. Eng. 31 (8), 1054–1064.
Domínguez, J.M., Fourtakas, G., Altomare, C., Canelas, R.B., Tafuni, A., García-al, O., Martínez-Estévez, I., Mokos, A., Vacondio, R., Crespo, A. J.C., et al., 2022. DualSPHysics: from fluid dynamics to multiphysics problems. Comput. Particle Mech. 9 (5), 867–895.
Flanagan, D.P., Belytschko, T., 1981. A uniform strain hexahedron and quadrilateral with orthogonal hourglass control. Int. J. Numer. Methods Eng. 17 (5), 679–706.
Fourey, G., Hermange, C., Le Touzé, D., Oger, G., 2017. An efficient FSI coupling strategy between smoothed particle hydrodynamics and finite element methods. Comput. Phys. Commun. 217, 66–81.
Fuchs, S.L., Meier, C., Wall, W.A., Cyron, C.J., 2021. A novel smoothed particle hydrodynamics and finite element coupling scheme for fluid–structure interaction: the sliding boundary particle approach. Comput. Methods Appl. Mech. Eng. 383, 113922.
Gao, T., Fu, L., 2024. A three-dimensional meshless fluid–shell interaction framework based on smoothed particle hydrodynamics coupled with semi-meshless thin shell. Comput. Methods Appl. Mech. Eng. 429, 117179.
Gingold, R.A., Monaghan, J.J., 1977. Smoothed particle hydrodynamics: theory and application to non-spherical stars. Mon. Not. R. Astron. Soc. 181 (3), 375–389.
Gotoh, H., Khayyer, A., Shimizu, Y., 2021. Entirely lagrangian meshfree computational methods for hydroelastic fluid-structure interactions in ocean engineering–reliability, adaptivity and generality. Appl. Ocean Res. 115, 102822.
Groenenboom, P., Cartwright, B., McGuckin, D., Amoignon, O., Mettichi, M.Z., Gargouri, Y., Kamoulakos, A., 2019. Numerical studies and industrial applications of the hybrid SPH-FE method. Comput. Fluids 184, 40–63.
Groenenboom, P., Siemann, M., 2015. Fluid-structure interaction by the mixed SPH-FEM method with application to aircraft ditching. Int. J. Multiphys. 9 (3), 249–266.
Guan, X., Zhao, W., Wan, D., Xu, i., Liu, J., 2023. Numerical simulations of complex water spray flows around aircraft landing tire. Eur. J. Mech.-B/Fluids 97, 28–39.
Guan, X.-S., Sun, P.-N., Xu, Y., Lyu, H.-G., Geng, L.-M., 2024a. Numerical studies of complex fluid-solid interactions with a six degrees of freedom quaternion-based solver in the SPH framework. Ocean Eng. 291, 116484.
Guan, X.-S., Sun, P.-N., Zhang, X., Lyu, H.-G., Xu, Y., 2024b. Sph simulations of complex 3d fluid–solid interactions with an improved single-layer particle boundary technique preventing boundary penetration. Ocean Eng. 312, 119061.
Hasanpour, A., Istrati, D., Buckle, I., 2021. Coupled SPH–FEM modeling of tsunami-borne large debris flow and impact on coastal structures. J. Mar. Sci. Eng. 9 (10), 1068.
Hermange, C., Oger, G., Le Chenadec, Y., Le Touzé, D., 2019. A 3d SPH-FEM coupling for FSI problems and its application to tire hydroplaning simulations on rough ground. Comput. Methods Appl. Mech. Eng. 355, 558–590.
Huang, C., Long, T., Liu, M., 2019. Coupling finite difrence method with finite particle method for modeling viscous incompressible flows. Int. J. Numer. Methods Fluids 90 (11), 564–583.
Huebner, K.H., Dewhirst, D.L., Smith, D.E., Byrom, T.G., 2001. The finite element method for engineers. John Wiley & Sons.
Hwang, S.-C., Park, J.-C., Gotoh, H., Khayyer, A., Kang, K.-J., 2016. Numerical simulations of sloshing flows with elastic baffles by using a particle-based fluid–structure interaction analysis method. Ocean Eng. 118, 227–241.

Jacob, B., Drawert, B., Yi, T.-M., Petzold, L., 2021. An arbitrary lagrangian eulerian smoothed particle hydrodynamics (ALE-SPH) method with a boundary volume fraction formulation for fluid-structure interaction. Eng. Anal. Bound. Elem. 128, 274–289.
Johnson, G.R., 1994. Linking of lagrangian particle methods to standard finite element methods for high velocity impact computations. Nucl. Eng. Des. 150 (2–3), 265–274.
Karmakar, S., Shaw, A., 2021. Response of RC plates under blast loading using FEM-SPH coupled method. Eng. Fail Anal. 125, 105409.
Khayyer, A., Gotoh, H., Falahaty, H., Shimizu, Y., 2018a. An enhanced ISPH-SPH coupled method for simulation of incompressible fluid–elastic structure interactions. Comput. Phys. Commun. 232, 139–164.
Khayyer, A., Gotoh, H., Falahaty, H., Shimizu, Y., 2018b. Towards development of enhanced fully-lagrangian mesh-free computational methods for fluid-structure interaction. J. Hydrodyn. 30, 49–61.
Khayyer, A., Gotoh, H., Shimizu, Y., 2022a. On systematic development of FSI solvers in the context of particle methods. J. Hydrodyn. 34 (3), 395–407.
Khayyer, A., Shimizu, Y., Gotoh, H., Hattori, S., 2021. Multi-resolution ISPH-SPH for accurate and efficient simulation of hydroelastic fluid-structure interactions in ocean engineering. Ocean Eng. 226, 108652.
Khayyer, A., Shimizu, Y., Gotoh, H., Hattori, S., 2022b. A 3d SPH-based entirely lagrangian meshfree hydroelastic FSI solver for anisotropic composite structures. Appl. Math. Model. 112, 560–613.
Kjellgren, P., Hyvärinen, J., 1998. An arbitrary lagrangian-eulerian finite element method. Comput. Mech. 21 (1), 81–90.
Li, G., Gao, J., Wen, P., Zhao, Q., Wang, J., Yan, J., Yamaji, A., 2020. A review on MPS method developments and applications in nuclear engineering. Comput. Methods Appl. Mech. Eng. 367, 113166.
Li, H., Han, B., Liu, S., Chen, S., Wang, Z., Deng, B., 2024. A review of the numerical strategies for solving ship hydroelasticity based on CFD-FEM technology. Ships Offshore Struct. 19 (11), 1912–1930.
Liang, G.-Q., Sun, P.-N., Lyu, H.-G., Zhang, G.-Y., 2025. A coupled $\delta+$-SPH-NOSB-PD method: towards fluid-structure interaction problems involving violent free-surface flows and isotropic structural linear elastic deformations and failures. Appl. Math. Model. 145, 116104.
Liu, M., Zhang, Z., 2019. Smoothed particle hydrodynamics (SPH) for modeling fluid-structure interactions. Sci. China Phys. Mech. Astronomy 62, 1–38.
Liu, M.B., Liu, G., 2010. Smoothed particle hydrodynamics (SPH): an overview and recent developments. Arch. Comput. Methods Eng. 17 (1), 25–76.
Liu, X., Yang, Y., Yang, Q., Xu, F., 2025. A robust low-dissipation riemann-SPH solver with a novel hybrid boundary treatment method for FSI problems. J. Fluids Struct. 135, 104316.
Lucy, L.B., 1977. A numerical approach to the testing of the fission hypothesis. Astron. J. (N. Y.) 82, 1013–1024.
Lyu, H.-G., Deng, R., Sun, P.-N., Miao, J.-M., 2021. Study on the wedge penetrating fluid interfaces characterized by difrent density-ratios: numerical investigations with a multi-phase SPH model. Ocean Eng. 237, 109538.
Lyu, H.-G., Sun, P.-N., Huang, X.-T., Liu, M.-B., Zha, H.-Y., Zhang, A.-M., 2024. Numerical investigation of vehicle wading based on an entirely particle-based three-dimensional SPH model. Comput. Fluids 270, 106144.
Lyu, H.-G., Sun, P.-N., Miao, J.-M., Zhang, A.-M., 2022. 3D multi-resolution SPH modeling of the water entry dynamics of free-fall liboats. Ocean Eng. 257, 111648.
Marrone, S., Di Mascio, A., Le Touzé, D., 2016. Coupling of smoothed particle hydrodynamics with finite volume method for free-surface flows. J. Comput. Phys. 310, 161–180.
Monaghan, J.J., 2005. Smoothed particle hydrodynamics. Rep. Prog. Phys. 68 (8), 1703–1759. cited By 1756.
Monaghan, J.J., Gingold, R.A., 1983. Shock simulation by the particle method SPH. J. Comput. Phys. 52 (2), 374–389.
Peng, Y.-X., Zhang, A.-M., Wang, S.-P., 2021. Coupling of WCSPH and RKPM for the simulation of incompressible fluid–structure interactions. J. Fluids Struct. 102, 103254.
Qian, L., Zhang, X., 1995. Rigid finite element and its applications in engineering. Acta Mech. Sin. 11 (1), 44–50.
Saha, S., Karmakar, S., 2025. Assessments and preventions of the damages and their modes in the second and third spans of the RC highway straight girder bridge under surface blast using the FEM-SPH coupling. Eng. Anal. Bound. Elem. 175, 106201.
Scolan, Y.-M., 2004. Hydroelastic behaviour of a conical shell impacting on a quiescent-free surface of an incompressible liquid. J. Sound Vib. 277 (1–2), 163–203.
Shi, H.-T., Yuan, G.-Y., Ni, B.-Y., Zhang, L.-W., 2024. Quasi-brittle ice breaking mechanisms by high-velocity water jet impacts: an investigation based on PD-SPH coupling model and experiments. J. Mech. Phys. Solids 191, 105783.
Shi, W.-K., Chen, C., Peng, Y.-X., Shen, Y.-M., Chen, J.-Q., Liu, M.-B., 2026. A 3d multi-resolution SPH-FEM coupling model with boundary penetration prevention technique for violent fluid-structure interactions. Comput. Methods Appl. Mech. Eng. 449, 118546.
Shimizu, Y., Khayyer, A., Gotoh, H., 2022. An implicit SPH-based structure model for accurate fluid–structure interaction simulations with hourglass control scheme. Eur. J. Mech.-B/Fluids 96, 122–145.
Siemann, M.H., Langrand, B., 2017. Coupled fluid-structure computational methods for aircraft ditching simulations: comparison of ALE-FE and SPH-FE approaches. Comput. Struct. 188, 95–108.
Sun, P.-N., Le Touze, D., Oger, G., Zhang, A.-M., 2021. An accurate FSI-SPH modeling of challenging fluid-structure interaction problems in two and three dimensions. Ocean Eng. 221, 108552.
Sun, P.N., Pilloton, C., Antuono, M., Colagrossi, A., 2023. Inclusion of an acoustic damper term in weakly-compressible SPH models. J. Comput. Phys. , 112056.
Sun, Z., Djidjeli, K., Xing, J.T., 2017. The weak coupling between MPS and BEM for wave structure interaction simulation. Eng. Anal. Bound. Elem. 82, 111–118.
Topalović, M., Nikolić, A., Vulović, S., Milovanović, V.P., 2021. Fsi analysis with continuous fluid flow using fem and sph methods in ls-dyna. J. Serbian Soc. Comput. Mech./Vol 15 (2), 93–100.
Vacondio, R., Altomare, C., De Leffe, M., Hu, X., Le Touzé, D., Lind, S., Marongiu, J.-C., Marrone, S., Rogers, B.D., Souto-Iglesias, A., 2021. Grand challenges for smoothed particle hydrodynamics numerical schemes. Comput. Particle Mech. 8 (3), 575–588.
Wendland, H., 1995. Piecewise polynomial, positive definite and compactly supported radial functions of minimal degree. Adv. Comput. Math. 4, 389–396.
Wu, H., Li, Y., Gu, S., 2025. Study on the thermal stress characteristics of ice covers in cold-region channels based on smoothed particle hydrodynamics. Phys. Fluids 37 (4).
Wu, S.R., Gu, L., 2012. Introduction to the explicit finite element method for nonlinear transient dynamics. John Wiley & Sons.
Xu, X., Wang, X., Tian, L., Yu, P., 2025. Three-dimensional SPH simulations of transient viscoelastic fluid flows with a level-set based pre-processing algorithm: towards industrial applications. Eng. Anal. Bound. Elem. 179, 106330.
Yao, C., Xu, C., Zhou, X., Liu, Q., Qiang, B., 2024. Study on the destruction process of piers by debris flow impact using SPH-FEM adaptive coupling method. KSCE J. Civ. Eng. 28 (8), 3162–3175.
Yao, X., Zhang, X., Huang, D., 2023. An improved SPH-FEM coupling approach for modeling fluid–structure interaction problems. Comput. Particle Mech. 10 (2), 313–330.
Zhang, A.-M., Sun, P.-N., Ming, F.-R., Colagrossi, A., 2017. Smoothed particle hydrodynamics and its applications in fluid-structure interactions. J. Hydrodyn., Ser. B 29 (2), 187–216.
Zhang, C., Rezavand, M., Hu, X., 2021a. A multi-resolution SPH method for fluid-structure interactions. J. Comput. Phys. 429, 110028.
Zhang, G., ng, S., Zhang, Z., Chen, Y., Sun, Z., Zong, Z., 2021b. Investigation of hydroelasticity in water entry of flexible wedges with flow detachment. Ocean Eng. 222, 108580.
Zhang, G., Yang, X., Liang, G., Zheng, K., Zhang, Z., 2024. Numerical simulation of sloshing flows with elastic structure by coupling $\delta+$-SPH and SPIM. Eng. Anal. Bound. Elem. 165, 105764.
Zhang, G., Zhao, W., Wan, D., 2022. Moving particle semi-implicit method coupled with finite element method for hydroelastic responses of floating structures in waves. Eur. J. Mech.-B/Fluids 95, 63–82.
Zhang, Z., Qiang, H., Gao, W., 2011. Coupling of smoothed particle hydrodynamics and finite element method for impact dynamics simulation. Eng. Struct. 33 (1), 255–264.
Zhang, Z.L., Khalid, M., Long, T., Liu, M.B., Shu, C., 2021c. Improved element-particle coupling strategy with δ-SPH and particle shifting for modeling sloshing with rigid or deformable structures. Appl. Ocean Res. 114, 102774.